



# A face-based smoothed finite element method (FS-FEM) for visco-elastoplastic analyses of 3D solids using tetrahedral mesh

T. Nguyen-Thoi<sup>a,c,\*</sup>, G.R. Liu<sup>a,b</sup>, H.C. Vu-Do<sup>a,c</sup>, H. Nguyen-Xuan<sup>b,c</sup>

<sup>a</sup> Center for Advanced Computations in Engineering Science (ACES), Department of Mechanical Engineering, National University of Singapore, 9 Engineering Drive 1, Singapore 117576, Singapore

<sup>b</sup> Singapore-MIT Alliance (SMA), E4-04-10, 4 Engineering Drive 3, Singapore 117576, Singapore

<sup>c</sup> Faculty of Mathematics and Computer Science, University of Science, Vietnam National University-HCM, Viet Nam

## ARTICLE INFO

### Article history:

Received 27 April 2009

Received in revised form 27 June 2009

Accepted 8 July 2009

Available online 12 July 2009

### Keywords:

Numerical methods

Meshfree methods

Face-based smoothed finite element method (FS-FEM)

Finite element method (FEM)

Strain smoothing technique

Visco-elastoplastic analyses

## ABSTRACT

A face-based smoothed finite element method (FS-FEM) using tetrahedral elements was recently proposed to improve the accuracy and convergence rate of the existing standard finite element method (FEM) for the solid mechanics problems. In this paper, the FS-FEM is further extended to more complicated visco-elastoplastic analyses of 3D solids using the von-Mises yield function and the Prandtl–Reuss flow rule. The material behavior includes perfect visco-elastoplasticity and visco-elastoplasticity with isotropic hardening and linear kinematic hardening. The formulation shows that the bandwidth of stiffness matrix of FS-FEM is larger than that of FEM, and hence the computational cost of FS-FEM in numerical examples is larger than that of FEM for the same mesh. However, when the efficiency of computation (computation time for the same accuracy) in terms of a posteriori error estimation is considered, the FS-FEM is more efficient than the FEM.

© 2009 Elsevier B.V. All rights reserved.

## 1. Introduction

Recently years, significant development has been made in meshfree methods in term of theory, formulism and application [1]. Some of these meshfree techniques have been applied back to finite element settings [2]. The strain smoothing technique has been proposed by Chen et al. [3] to stabilize the solutions of the nodal integrated meshfree methods and then applied in the natural-element method [4]. Liu et al. has generalized the gradient (strain) smoothing technique [5] and applied it in the meshfree context [6–13] to formulate the node-based smoothed point interpolation method (NS-PIM or LC-PIM) [14,15] and the node-based smoothed radial point interpolation method (NS-RPIM or LC-RPIM) [16]. Applying the same idea to the FEM, a cell-based smoothed finite element method (SFEM or CS-FEM) [17–20], a node-based smoothed finite element method (NS-FEM) [21] and an edge-based smoothed finite element method (ES-FEM) in two-dimensional (2D) problems [22] have also been formulated.

In the CS-FEM, the domain discretization is still based on quadrilateral elements as in the FEM, however the stiffness matrices are calculated based over smoothing cells (SC) located inside the quadrilateral elements as shown in Fig. 1. When the number of SC of the elements equals 1, the CS-FEM solution has the same properties with those of FEM using reduced integration. The CS-FEM in this case can be unstable and can have spurious zeros energy modes, depending on the setting of the problem. A stabilization technique to alleviate this instability can be found in ref [27] which can be extended for 3D finite elements and for plasticity problems. When SC approaches infinity, the CS-FEM solution approaches to the solution of the standard displacement compatible FEM model [18]. In practical calculation, using four smoothing cells for each quadrilateral element in the CS-FEM is easy to implement, work well in general and hence advised for all problems. The numerical solution of CS-FEM (SC = 4) is always stable, accurate, much better than that of FEM, and often very close to the exact solutions. The CS-FEM has been extended for general  $n$ -sided polygonal elements ( $n$ SFEM or  $n$ CS-FEM) [28], dynamic analyses [29], incompressible materials using selective integration [30,31], plate and shell analyses [32–36], and further extended for the extended finite element method (XFEM) to solve fracture mechanics problems in 2D continuum and plates [37].

In the NS-FEM, the domain discretization is also based on elements as in the FEM, however the stiffness matrices are calculated

\* Corresponding author. Address: Department of Mechanics, Faculty of Mathematics and Computer Science, University of Science, Vietnam National University-HCM, Vietnam, 227 Nguyen Van Cu street, District 5, Hochiminh city, Viet Nam. Tel.: + 84 (0)942340411.

E-mail addresses: [ngttrung@hcmuns.edu.vn](mailto:ngttrung@hcmuns.edu.vn), [thoitruong76@yahoo.com](mailto:thoitruong76@yahoo.com) (T. Nguyen-Thoi).

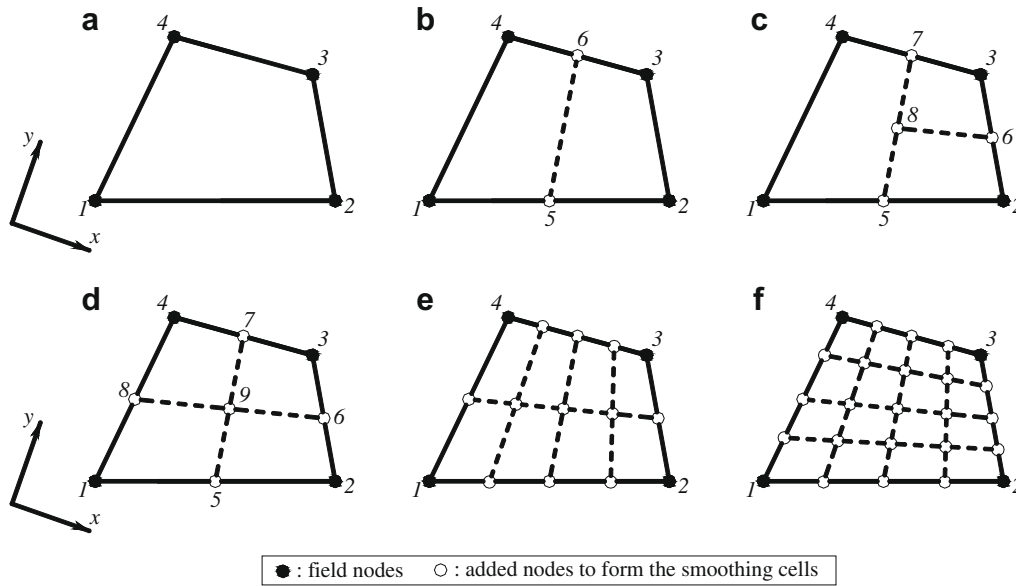


Fig. 1. Division of quadrilateral element into the smoothing cells (SCs) in CS-FEM by connecting the mid-segment-points of opposite segments of smoothing cells. (a) 1 SC; (b) 2 SCs; (c) 3 SCs; (d) 4 SCs; (e) 8 SCs; and (f) 16 SCs.

based on smoothing domains associated with nodes. The NS-FEM works well for triangular elements, and can be applied easily to general  $n$ -sided polygonal elements [21] for 2D problems and tetrahedral elements for 3D problems. For  $n$ -sided polygonal elements [21], smoothing domain  $\Omega^{(k)}$  associated with the node  $k$  is created by connecting sequentially the mid-edge-point to the central points of the surrounding  $n$ -sided polygonal elements of the node  $k$  as shown in Fig. 2. Note that  $n$ -sided polygonal elements were also formulated in standard FEM settings [38–41]. When only linear triangular or tetrahedral elements are used, the NS-FEM produces the same results as the method proposed by Dohrmann et al. [42] or to the NS-PIM (or LC-PIM) [14] using linear interpolation. The NS-FEM [21] has been found immune naturally from volumetric locking and possesses the upper bound property in strain energy as presented in [43]. Hence, by combining the NS-FEM and FEM with a scale factor  $\alpha \in [0, 1]$ , a new method named as the al-

pha Finite Element Method ( $\alpha$ FEM) [44] is proposed to obtain nearly exact solutions in strain energy using triangular and tetrahedral elements. The  $\alpha$ FEM [44] is therefore also a good candidate among the methods having super convergence and high efficiency in non-linear problems [45–47]. The NS-FEM has been developed for adaptive analysis [48]. One disadvantage of NS-FEM is its larger bandwidth of stiffness matrix compared to that of FEM, because the number of nodes related to the smoothing domains associated with nodes is larger than that related to the elements. The computational cost of NS-FEM therefore is larger than that of FEM for the same meshes used. In terms of computational efficiency (CPU time needed for the same accuracy results measured in energy norm), however, the NS-FEM-T3 can be much better than the FEM-T3 (see, Chapter 8 in [1]).

In the ES-FEM [22], the problem domain is also discretized using triangular elements as in the FEM, however the stiffness matrices are calculated based on smoothing domains associated with the edges of the triangles. For triangular elements, the smoothing domain  $\Omega^{(k)}$  associated with the edge  $k$  is created by connecting two endpoints of the edge to the centroids of the adjacent elements as shown in Fig. 3. The numerical results of ES-FEM using examples of static, free and forced vibration analyses of solids [22] demonstrated the following excellent properties: (1) the ES-FEM is often found super-convergent and much more accurate than the FEM using triangular elements (FEM-T3) and even more accurate than the FEM using quadrilateral elements (FEM-Q4) with the same sets of nodes; (2) there are no spurious non-zeros energy modes and hence the ES-FEM is both spatial and temporal stable and works well for vibration analysis; (3) no additional degree of freedom and no penalty parameter is used; (4) a novel domain-based selective scheme is proposed leading to a combined ES/NS-FEM model that is immune from volumetric locking and hence works very well for nearly incompressible materials. Note that similar to the NS-FEM, the bandwidth of stiffness matrix in the ES-FEM is larger than that in the FEM-T3, hence the computational cost of ES-FEM is larger than that of FEM-T3. However, when the efficiency of computation (computation time for the same accuracy) in terms of both energy and displacement error norms is considered, the ES-FEM is more efficient [22]. The ES-FEM has been developed for 2D piezoelectric [23], 2D visco-elastoplastic [24], plate [25] and primal-dual shakedown analyses [26].

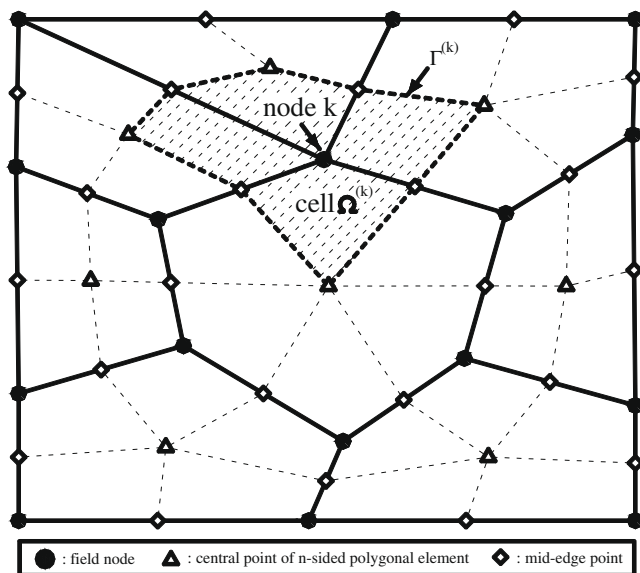


Fig. 2.  $n$ -Sided polygonal elements and the smoothing cell (shaded area) associated with nodes in NS-FEM.

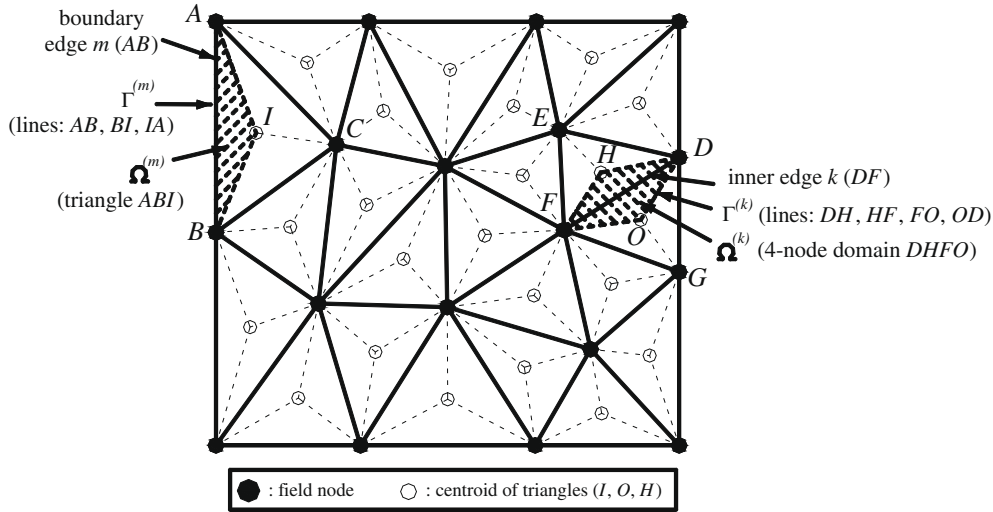


Fig. 3. Triangular elements and the smoothing domains (shaded areas) associated with edges in ES-FEM.

Further more, the idea of ES-FEM has been extended for the 3D problems using tetrahedral elements to give a so-called the face-based smoothed finite element method (FS-FEM) [49]. In the FS-FEM, the domain discretization is still based on tetrahedral elements as in the FEM, however the stiffness matrices are calculated based on smoothing domains associated with the faces of the tetrahedral elements as shown in Fig. 4. The FS-FEM is found significantly more accurate than the FEM using tetrahedral elements for both linear and geometrically non-linear solid mechanics problems. In addition, a novel domain-based selective scheme is proposed leading to a combined FS/NS-FEM model that is immune from volumetric locking and hence works well for nearly incompressible materials. The implementation of the FS-FEM is straightforward and no penalty parameters or additional degrees of freedom are used. Note that similar to the ES-FEM and NS-FEM, the bandwidth of stiffness matrix in the FS-FEM is also larger than that in the FEM, and hence the computational cost of FS-FEM is larger than that of FEM. However, when the efficiency of computation (computation time for the same accuracy) in terms of both energy and displacement error norms is considered, the FS-FEM is still more efficient than the FEM [49].

In this paper, we aim to extend the FS-FEM to even more complicated visco-elastoplastic analyses in 3D solids. In this work, we combine the FS-FEM with the work of Carstensen and Klose [50] using the standard FEM in the setting of von-Mises conditions

and a Prandtl–Reuss flow rule. The material behavior includes perfect visco-elastoplasticity and visco-elastoplasticity with isotropic hardening and linear kinematic hardening in a dual model with both displacements and the stresses as the main variables. The numerical procedure, however, eliminates the stress variables and the problem becomes only displacement-dependent and is easier to deal with. The formulation shows that the bandwidth of stiffness matrix of FS-FEM is larger than that of FEM, and hence the computational cost of FS-FEM in numerical examples is larger than that of FEM. However, when the efficiency of computation (computation time for the same accuracy) in terms of a posteriori error estimation is considered, the FS-FEM is more efficient than the FEM.

## 2. Dual model of visco-elastoplastic problem using the FS-FEM

### 2.1. Strong form and weak form [50]

The visco-elastoplastic problem which deforms in the interval  $t \in [0, T]$  can be described by equilibrium equation in the domain  $\Omega$  bounded by  $\Gamma$

$$\text{div} \sigma + \mathbf{b} = \mathbf{0} \text{ in } \Omega \tag{1}$$

where  $\mathbf{b} \in (\mathbb{L}_2(\Omega))^3$  is the body forces,  $\sigma \in (\mathbb{L}_2(\Omega))^3$  is the stress field. The essential and static boundary conditions, respectively, on the Dirichlet boundary  $\Gamma_D$  and the Neumann boundary  $\Gamma_N$  are

$$\mathbf{u} = \mathbf{w}_0 \text{ on } \Gamma_D \text{ and } \sigma \mathbf{n} = \bar{\mathbf{t}} \text{ on } \Gamma_N \tag{2}$$

in which  $\mathbf{u} \in (\mathbb{H}^1(\Omega))^3$  is the displacement field;  $\mathbf{w}_0 \in (\mathbb{H}^1(\Omega))^3$  is prescribed surface displacement;  $\bar{\mathbf{t}} \in (\mathbb{L}_2(\Gamma_N))^3$  is prescribed surface force and  $\mathbf{n}$  is the unit outward normal matrix.

In the context of small strain, the total strain  $\varepsilon(\mathbf{u}) = \nabla_S \mathbf{u}$ , where  $\nabla_S \mathbf{u}$  denotes the symmetric part of displacement gradient, is separated into two contributions

$$\varepsilon(\mathbf{u}) = \mathbf{e}(\sigma) + \mathbf{p}(\xi) \tag{3}$$

where  $\mathbf{e}(\sigma) = \mathbf{C}^{-1} \sigma$  is elastic strain tensor;  $\xi$  is internal variable and  $\mathbf{p}(\xi)$  is an irreversible plastic strain in which  $\mathbf{C}$  is a fourth order tensor of material constants.

To describe properly the evolution process for the plastic strain, it is required to define the admissible stresses, a yield function, and an associated flow rule. In this work, we use the von-Mises yield function and the Prandtl–Reuss flow rule. Let  $\mathbf{p}$  and  $\xi$  be the kinematic variables of the generalized strain  $\mathbf{P} = (\mathbf{p}, \xi)$ , and  $\Sigma = (\sigma, \alpha)$

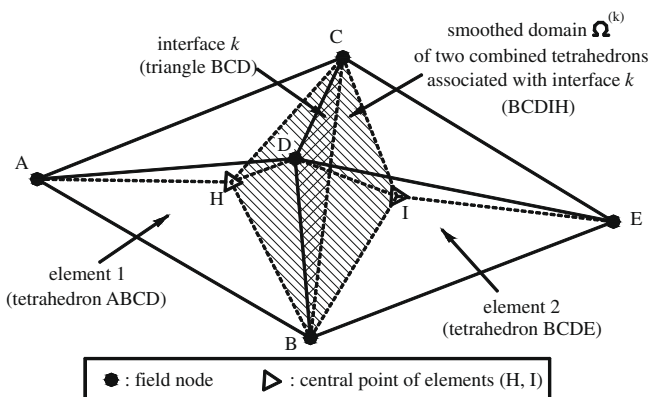


Fig. 4. Two adjacent tetrahedral elements and the smoothing domain  $\Omega^{(k)}$  (shaded domain) formed based on their interface  $k$  in the FS-FEM

be the corresponding generalized stress, where  $\alpha$  is the hardening parameter describing internal stresses. We define  $\mathcal{Y}$  to be the admissible stresses set, which is a closed, convex set, containing 0, and defined by

$$\mathcal{Y} = \{ \Sigma : \Phi(\Sigma) \leq 0 \} \tag{4}$$

where  $\Phi$  is the von-Mises yield function which is presented specifically for different visco-elastoplasticity cases as follows:

Case a: Perfect visco-elastoplasticity:

In this case, there is no hardening and the internal variables  $\xi, \alpha$  are absent. The von-Mises yield function is given simply by

$$\Phi(\sigma) = \|\text{dev}(\sigma)\| - \sigma_Y \tag{5}$$

where  $\sigma_Y$  is the yield stress;  $\|\mathbf{x}\|$  is the norm of tensor  $\mathbf{x}$  and is computed by  $\|\mathbf{x}\| = \sqrt{\sum_{i=1}^3 \sum_{j=1}^3 \mathbf{x}_{ij}^2}$ ,  $\text{dev}(\mathbf{x})$  is the deviator tensor of tensor  $\mathbf{x}$  and defined by

$$\text{dev}(\mathbf{x}) = \mathbf{x} - \frac{\text{tr}(\mathbf{x})}{3} \mathbf{I} \tag{6}$$

in which  $\mathbf{I}$  is the second-order symmetric unit tensor and  $\text{tr}(\mathbf{x}) = \sum_{i=1}^3 \mathbf{x}_{ii}$  is the trace operator of tensor  $\mathbf{x}$ . For the viscosity parameter  $\nu > 0$ , the Prandtl–Reuss flow rule has the form

$$\dot{\mathbf{p}} = \begin{cases} \frac{1}{\nu} (\|\text{dev}(\sigma)\| - \sigma_Y) & \text{if } \|\text{dev}(\sigma)\| > \sigma_Y \\ 0 & \text{if } \|\text{dev}(\sigma)\| \leq \sigma_Y \end{cases} \tag{7}$$

Case b: Visco-elastoplasticity with isotropic hardening:

In the case of the isotropic hardening, the problem is characterized by a modulus of hardening  $H \geq 0$ , and  $\alpha \equiv \alpha^I \geq 0$  ( $I$  means Isotropic) becomes a scalar hardening parameter and relates to the scalar internal strain variable  $\xi$  by

$$\alpha^I = -H_1 \xi \tag{8}$$

where  $H_1$  is a positive hardening parameter.

The von-Mises yield function is given by

$$\Phi(\sigma, \alpha^I) = \|\text{dev}(\sigma)\| - \sigma_Y(1 + H\alpha^I) \tag{9}$$

For the viscosity parameter  $\nu > 0$ , the Prandtl–Reuss flow rule has the form

$$\begin{pmatrix} \dot{\mathbf{p}} \\ \dot{\xi} \end{pmatrix} = \begin{cases} \frac{1}{\nu(1+H^2\sigma_Y^2)} \begin{pmatrix} \|\text{dev}(\sigma)\| - (1+\alpha^I H)\sigma_Y \\ -H\sigma_Y(\|\text{dev}(\sigma)\| - (1+\alpha^I H)\sigma_Y) \end{pmatrix} & \text{if } \|\text{dev}(\sigma)\| > (1+\alpha^I H)\sigma_Y \\ \begin{pmatrix} 0 \\ 0 \end{pmatrix} & \text{if } \|\text{dev}(\sigma)\| \leq (1+\alpha^I H)\sigma_Y \end{cases} \tag{10}$$

Case c: Visco-elastoplasticity with linear kinematic hardening:

In the case of the linear kinematic hardening, the internal stress  $\alpha \equiv \alpha^K$  ( $K$  means Kinematic) relates to the internal strain  $\xi$  by

$$\alpha^K = -k_1 \xi \tag{11}$$

where  $k_1$  is a positive parameter.

The von-Mises yield function is given by

$$\Phi(\sigma, \alpha^K) = \|\text{dev}(\sigma) - \text{dev}(\alpha^K)\| - \sigma_Y \tag{12}$$

For the viscosity parameter  $\nu > 0$ , the Prandtl–Reuss flow rule has the form

$$\begin{pmatrix} \dot{\mathbf{p}} \\ \dot{\xi} \end{pmatrix} = \begin{cases} \frac{1}{2\nu} \begin{pmatrix} \|\text{dev}(\sigma - \alpha^K)\| - \sigma_Y \\ -(\|\text{dev}(\sigma - \alpha^K)\| - \sigma_Y) \end{pmatrix} & \text{if } \|\text{dev}(\sigma - \alpha^K)\| > \sigma_Y \\ \begin{pmatrix} 0 \\ 0 \end{pmatrix} & \text{if } \|\text{dev}(\sigma - \alpha^K)\| \leq \sigma_Y \end{cases} \tag{13}$$

In general, the Prandtl–Reuss flow rule, with the viscosity parameter  $\nu > 0$ , has the form [50]

$$\begin{pmatrix} \dot{\mathbf{p}} \\ \dot{\xi} \end{pmatrix} = \frac{1}{\nu} \begin{pmatrix} \sigma - \Pi\sigma \\ \alpha - \Pi\alpha \end{pmatrix} \tag{14}$$

where  $\Pi\sigma$  and  $\Pi\alpha$  are defined as the projections of  $(\sigma, \alpha)$  into the admissible stresses set  $\mathcal{Y}$ .

The visco-elastoplastic problem can now be stated generally in a weak formulation with the above-mentioned flow rules as follows: seek  $\mathbf{u} \in (\mathbb{H}^1(\Omega))^3$  such that  $\mathbf{u} = \mathbf{w}_0$  on  $\Gamma_D$  and for  $\forall \mathbf{v} \in (\mathbb{H}_0^1(\Omega))^3 = \{\mathbf{v} \in (\mathbb{H}^1(\Omega))^3 : \mathbf{v} = \mathbf{0} \text{ on } \Gamma_D\}$ , the following equations are satisfied:

$$\int_{\Omega} \sigma(\mathbf{u}) : \varepsilon(\mathbf{v}) d\Omega = \int_{\Omega} \mathbf{b} \cdot \mathbf{v} d\Omega + \int_{\Gamma_N} \bar{\mathbf{t}} \cdot \mathbf{v} d\Gamma \tag{15}$$

$$\begin{pmatrix} \dot{\mathbf{p}} \\ \dot{\xi} \end{pmatrix} = \begin{pmatrix} \varepsilon(\dot{\mathbf{u}}) - \mathbf{C}^{-1} \dot{\sigma} \\ \xi(\dot{\alpha}) \end{pmatrix} = \frac{1}{\nu} \begin{pmatrix} \sigma - \Pi\sigma \\ \alpha - \Pi\alpha \end{pmatrix} \tag{16}$$

where  $\mathbf{A} : \mathbf{B} = \sum_{j,k} \mathbf{A}_{jk} \mathbf{B}_{jk}$  denotes the scalar products of (symmetric) matrices.

### 2.2. Time-discretization scheme [50]

A generalized midpoint rule is used as the time-discretization scheme. In each time step, a spatial problem needs to be solved with given variables  $(\mathbf{u}(t), \sigma(t), \alpha(t))$  at time  $t_0$  denoted as  $(\mathbf{u}_0, \sigma_0, \alpha_0)$  and unknowns at time  $t_1 = t_0 + \Delta t$  denoted as  $(\mathbf{u}_1, \sigma_1, \alpha_1)$ . Time derivatives are replaced by backward difference quotients; for instance  $\dot{\mathbf{u}}$  is replaced by  $\frac{\mathbf{u}_0 - \mathbf{u}_1}{\Delta t}$  where  $\mathbf{u}_\vartheta = (1 - \vartheta)\mathbf{u}_0 + \vartheta\mathbf{u}_1$  with  $1/2 \leq \vartheta \leq 1$ . The time discrete problem now becomes: seek  $\mathbf{u}_\vartheta \in (\mathbb{H}^1(\Omega))^3$  that satisfied  $\mathbf{u}_\vartheta = \mathbf{w}_0$  on  $\Gamma_D$  and

$$\int_{\Omega} \sigma(\mathbf{u}_\vartheta) : \varepsilon(\mathbf{v}) d\Omega = \int_{\Omega} \mathbf{b}_\vartheta \cdot \mathbf{v} d\Omega + \int_{\Gamma_N} \bar{\mathbf{t}}_\vartheta \cdot \mathbf{v} d\Gamma, \forall \mathbf{v} \in (\mathbb{H}_0^1(\Omega))^3 \tag{17}$$

$$\frac{1}{\vartheta \Delta t} \begin{pmatrix} \varepsilon(\mathbf{u}_\vartheta - \mathbf{u}_0) - \mathbf{C}^{-1}(\sigma_\vartheta - \sigma_0) \\ \xi(\alpha_\vartheta, t_\vartheta) - \xi(\alpha_0, t_0) \end{pmatrix} = \frac{1}{\nu} \begin{pmatrix} \sigma_\vartheta - \Pi\sigma_\vartheta \\ \alpha_\vartheta - \Pi\alpha_\vartheta \end{pmatrix} \tag{18}$$

where  $\mathbf{b}_\vartheta = (1 - \vartheta)\mathbf{b}_0 + \vartheta\mathbf{b}_1$ ,  $\bar{\mathbf{t}}_\vartheta = (1 - \vartheta)\bar{\mathbf{t}}_0 + \vartheta\bar{\mathbf{t}}_1$  in which  $\mathbf{b}_0, \bar{\mathbf{t}}_0, \mathbf{b}_1$  and  $\bar{\mathbf{t}}_1$  are body forces and surface forces at time  $t_0, t_1$ , respectively.

Eqs. (17) and (18) is in fact a dual model that has both stress and displacement as field variables. To solve the set of Eqs. (17) and (18) efficiently, we need to eliminate one variable. This can be done by first expressing explicitly the stress  $\sigma_\vartheta$  in the form of displacement  $\mathbf{u}_\vartheta$  using Eq. (18), and then substituting it into Eq. (17). The problem will then become only displacement-dependent, and we need to solve the resultant form of Eq. (17).

### 2.3. Analytic expression of the stress tensor

Explicit expressions for the stress tensor  $\sigma_\vartheta$  in different cases of visco-elastoplasticity can be presented briefly as follows [50]

(a) Perfect visco-elastoplasticity:

In the elastic phase

$$\sigma_\vartheta = C_1 \text{tr}(\vartheta \Delta t \mathbf{A}) \mathbf{I} + 2\mu \text{dev}(\vartheta \Delta t \mathbf{A}) \tag{19}$$

where  $\mathbf{A} = \frac{\varepsilon(\mathbf{u}_\vartheta - \mathbf{u}_0)}{\vartheta \Delta t} + \mathbf{C}^{-1} \frac{\sigma_0 - \sigma_\vartheta}{\vartheta \Delta t}$ .

In the plastic phase, the plastic occurs when  $\|\text{dev}(\vartheta \Delta t \mathbf{A})\| > \beta \sigma_Y$  and

$$\sigma_\vartheta = C_1 \text{tr}(\vartheta \Delta t \mathbf{A}) \mathbf{I} + (C_2 + C_3 / \|\text{dev}(\vartheta \Delta t \mathbf{A})\|) \text{dev}(\vartheta \Delta t \mathbf{A}) \tag{20}$$

where

$$C_1 = \lambda + 2\mu/3, C_2 = \nu / (\beta \nu + \vartheta \Delta t), C_3 = \vartheta \Delta t \sigma_Y / (\beta \nu + \vartheta \Delta t) \tag{21}$$

in which  $\beta = 1/(2\mu)$ .

(b) Visco-elastoplasticity with isotropic hardening:

In the elastic phase

$$\sigma_\vartheta = C_1 \text{tr}(\vartheta \Delta t \mathbf{A}) \mathbf{I} + 2\mu \text{dev}(\vartheta \Delta t \mathbf{A}) \tag{22}$$

In the plastic phase, the plastic occurs when  $\|\text{dev}(\vartheta \Delta t \mathbf{A})\| > \beta(1 + \alpha_0^I H) \sigma_Y$  and

$$\sigma_\theta = C_1 \text{tr}(\vartheta\Delta t\mathbf{A})\mathbf{I} + (C_3/(C_2\|\text{dev}(\vartheta\Delta t\mathbf{A})\|) + C_4/C_2)\text{dev}(\vartheta\Delta t\mathbf{A}) \quad (23)$$

where

$$\begin{aligned} C_1 &= \lambda + 2\mu/3, C_2 = \beta\nu(1 + H^2\sigma_Y^2) + \vartheta\Delta t(1 + \beta H_1 H^2\sigma_Y^2) \\ C_3 &= \vartheta\Delta t\sigma_Y(1 + \alpha_0^I H), C_4 = H_1 H^2\vartheta\Delta t\sigma_Y^2 + \nu(1 + H^2\sigma_Y^2) \end{aligned} \quad (24)$$

in which  $\alpha_0^I$  is the initial scalar hardening parameter.

(c) Visco-elastoplasticity with linear kinematic hardening:  
In the elastic phase

$$\sigma_\theta = C_1 \text{tr}(\vartheta\Delta t\mathbf{A})\mathbf{I} + 2\mu \text{dev}(\vartheta\Delta t\mathbf{A}) \quad (25)$$

In the plastic phase, the plastic occurs when  $\|\text{dev}(\vartheta\Delta t\mathbf{A} - \beta\alpha_0^K)\| > \beta\sigma_Y$  and

$$\begin{aligned} \sigma_\theta &= C_1 \text{tr}(\vartheta\Delta t\mathbf{A})\mathbf{I} + (C_2 + C_3/\|\text{dev}(\vartheta\Delta t\mathbf{A} - \beta\alpha_0^K)\|)\text{dev}(\vartheta\Delta t\mathbf{A} - \beta\alpha_0^K) \\ &+ \text{dev}(\alpha_0^K) \end{aligned} \quad (26)$$

where

$$\begin{aligned} C_1 &= \lambda + 2\mu/3, C_2 = \frac{\vartheta\Delta tk_1 + 2\nu}{\vartheta\Delta t + \beta\vartheta\Delta tk_1 + \nu/\mu}, \\ C_3 &= \frac{\vartheta\Delta t\sigma_Y}{\vartheta\Delta t + \beta\vartheta\Delta tk_1 + \nu/\mu} \end{aligned} \quad (27)$$

in which  $\sigma_0^k$  is the initial internal stress.

Now, by replacing the stress  $\sigma_\theta$  described explicitly into Eq. (17), we obtain the only displacement-dependent problem and can apply different numerical methods to solve.

#### 2.4. Discretization in space using FEM

The domain  $\Omega$  is now discretized into  $N_e$  elements and  $N_n$  nodes such that  $\Omega = \bigcup_{e=1}^{N_e} \Omega_e$  and  $\Omega_i \cap \Omega_j = \emptyset, i \neq j$ . In the discrete version of (17), the spaces  $\mathbb{V} = (\mathbb{H}^1(\Omega))^3$  and  $\mathbb{V}_0 = (\mathbb{H}_0^1(\Omega))^3$  are replaced

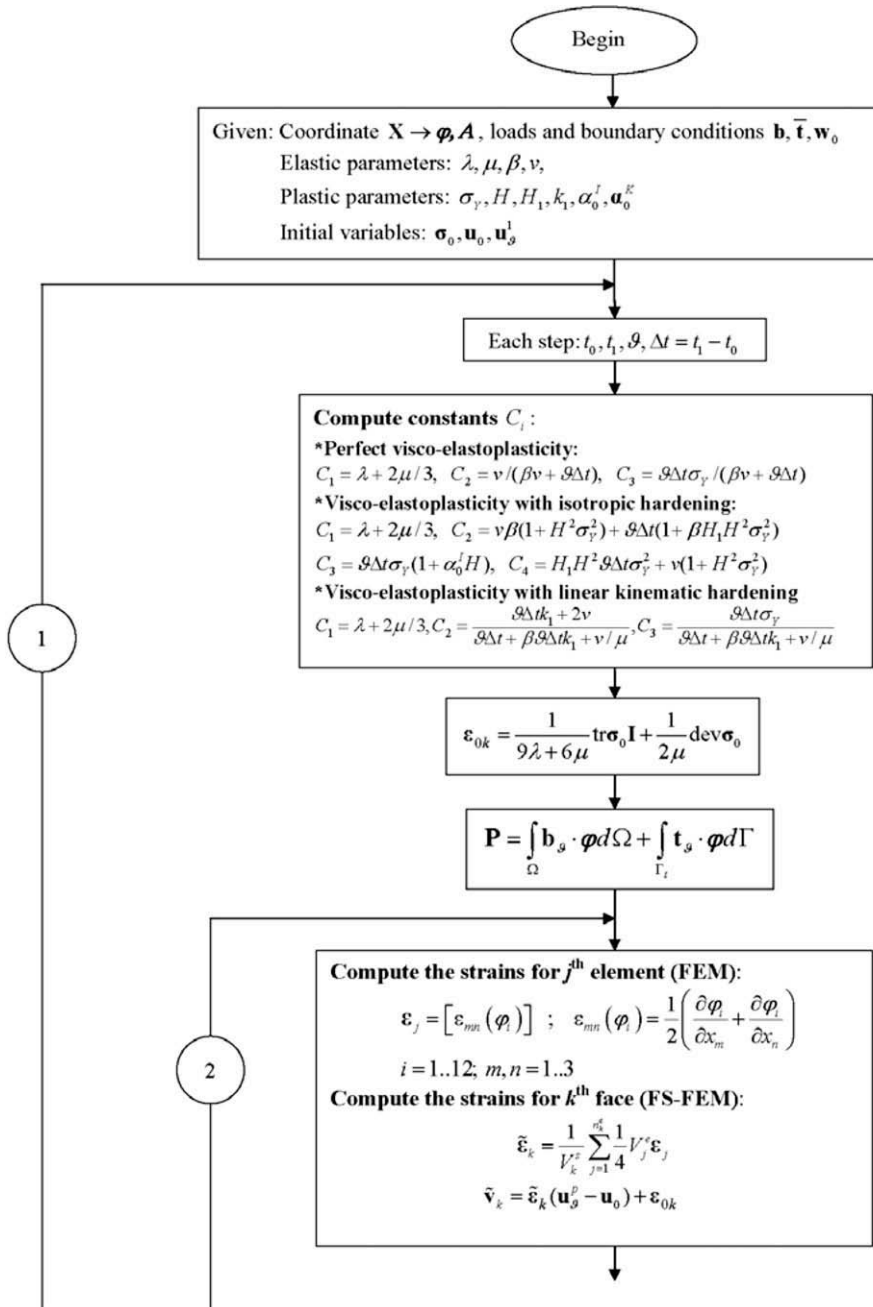


Fig. 5. Flow chart to solve the visco-elastoplastic problems using the FS-FEM: part 1.

by finite dimensional subspaces  $V^h \subset V$  and  $V_0^h \subset V_0$ . The discrete problem now becomes: seek  $\mathbf{u}_\theta \in V^h$  such that  $\mathbf{u}_\theta = \mathbf{w}_0$  on  $\Gamma_D$  and

$$\int_{\Omega} \sigma_\theta(\boldsymbol{\varepsilon}(\mathbf{u}_\theta - \mathbf{u}_0) + \mathbf{C}^{-1}\sigma_0) : \boldsymbol{\varepsilon}(\mathbf{v}) d\Omega = \int_{\Omega} \mathbf{b}_\theta \cdot \mathbf{v} d\Omega + \int_{\Gamma_N} \bar{\mathbf{t}}_\theta \cdot \mathbf{v} d\Gamma \quad \forall \mathbf{v} \in V_0^h \quad (28)$$

Let  $(\varphi_1, \dots, \varphi_{3N_n})$  be the nodal basis of the finite dimensional space  $V^h$ , where  $\varphi_i$  is the independent scalar hat shape function on node satisfying condition Kronecker  $\varphi_i(i) = 1$  and  $\varphi_i(j) = 0, i \neq j$ , then the discrete problem Eq. (28) now becomes: seeking  $\mathbf{u}_\theta \in V^h$  such that  $\mathbf{u}_\theta = \mathbf{w}_0$  on  $\Gamma_D$  and

$$\mathbf{F}_i = \int_{\Omega} \sigma_\theta(\boldsymbol{\varepsilon}(\mathbf{u}_\theta - \mathbf{u}_0) + \mathbf{C}^{-1}\sigma_0) : \boldsymbol{\varepsilon}(\varphi_i) d\Omega - \int_{\Omega} \mathbf{b}_\theta \cdot \varphi_i d\Omega - \int_{\Gamma_N} \bar{\mathbf{t}}_\theta \cdot \varphi_i d\Gamma = 0 \quad (29)$$

for  $i = 1, \dots, 3N_n$ .  $\mathbf{F}_i$  in Eq. (29) can be written in the sum of a part  $\mathbf{Q}_i$  which depends on  $\mathbf{u}_\theta$  and a part  $\mathbf{P}_i$  which is independent of  $\mathbf{u}_\theta$  such as

$$\mathbf{F}_i(\mathbf{u}_\theta) = \mathbf{Q}_i(\mathbf{u}_\theta) - \mathbf{P}_i \quad (30)$$

with

$$\mathbf{Q}_i(\mathbf{u}_\theta) = \mathbf{Q}_i = \int_{\Omega} \sigma_\theta(\boldsymbol{\varepsilon}(\mathbf{u}_\theta - \mathbf{u}_0) + \mathbf{C}^{-1}\sigma_0) : \boldsymbol{\varepsilon}(\varphi_i) d\Omega \quad (31)$$

$$\mathbf{P}_i = \int_{\Omega} \mathbf{b}_\theta \cdot \varphi_i d\Omega + \int_{\Gamma_N} \bar{\mathbf{t}}_\theta \cdot \varphi_i d\Gamma \quad (32)$$

2.5. Iterative solution

In order to solve Eq. (29) in this work, Newton–Raphson method is used [50]. In each step of the Newton iterations, the discrete

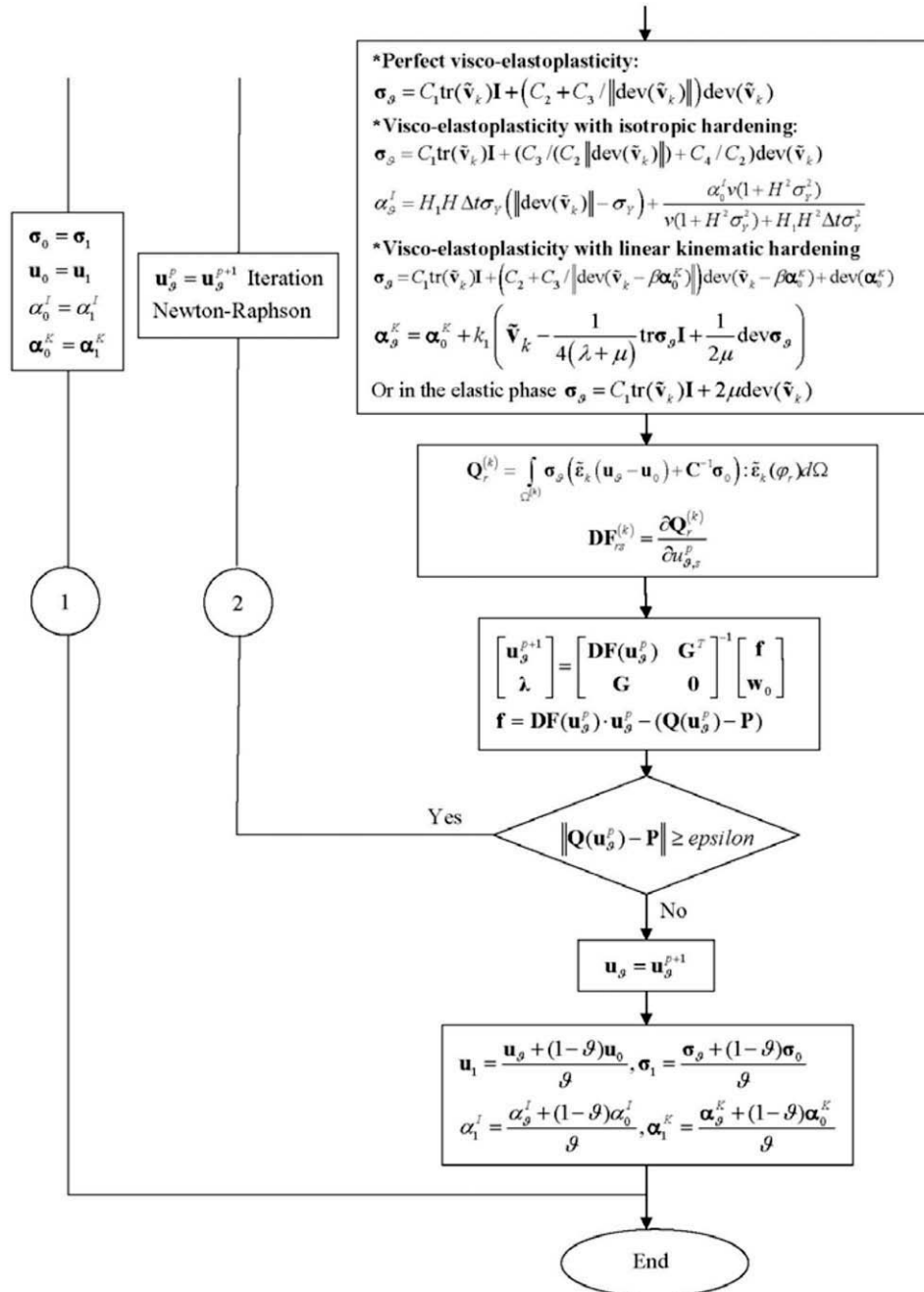
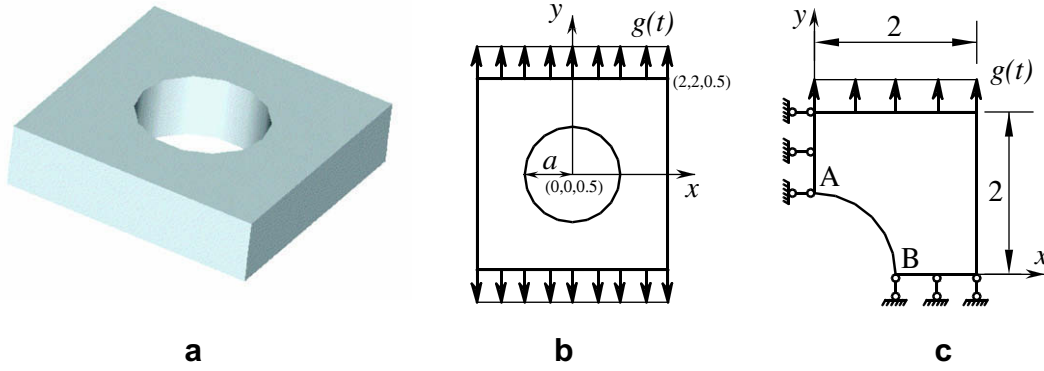


Fig. 6. Flow chart to solve the visco-elastoplastic problems using the FS-FEM: part 2.



**Fig. 7.** Thick plate with a cylindrical hole subjected to time dependent surface forces  $g(t)$  3D full model without forces; (b) model with forces viewed from the positive direction of  $z$ -axis; and (c) one eighth of model with forces and symmetric boundary conditions viewed from the positive direction of  $z$ -axis.

displacement vector  $\mathbf{u}_\theta^p$  expressed in the nodal basis by  $\mathbf{u}_\theta^p = \sum_{i=1}^{3N_n} \varphi_i u_i$  is determined from iterative solution

$$\mathbf{DF}(\mathbf{u}_\theta^p) \mathbf{u}_\theta^{p+1} = \mathbf{DF}(\mathbf{u}_\theta^p) \mathbf{u}_\theta^p - \mathbf{F}(\mathbf{u}_\theta^p) \quad (33)$$

where  $\mathbf{DF}$  is in fact the system stiffness matrix whose the local entries are defined as

$$\left( \mathbf{DF}(\mathbf{u}_{\theta,1}^p, \dots, \mathbf{u}_{\theta,3N_n}^p) \right)_{rs} = \partial \mathbf{F}_r(\mathbf{u}_{\theta,1}^p, \dots, \mathbf{u}_{\theta,3N_n}^p) / \partial u_{\theta,s}^p \quad (34)$$

where  $r, s \in \Psi_{df}$  which is the set containing degrees of freedom of all of nodes.

To properly apply the Dirichlet boundary conditions for our nonlinear problem, we use the approach of Lagrange multipliers. Combining the Newton iteration (33) and the set of boundary conditions imposed through Lagrange multipliers  $\lambda$ , the extended system of equations is obtained

$$\begin{pmatrix} \mathbf{DF}(\mathbf{u}_\theta^p) & \mathbf{G}^T \\ \mathbf{G} & \mathbf{0} \end{pmatrix} \begin{pmatrix} \mathbf{u}_\theta^{p+1} \\ \lambda \end{pmatrix} = \begin{pmatrix} \mathbf{f} \\ \mathbf{w}_0 \end{pmatrix} \quad (35)$$

with  $\mathbf{f} = \mathbf{DF}(\mathbf{u}_\theta^p) \mathbf{u}_\theta^p - \mathbf{F}(\mathbf{u}_\theta^p)$  and  $\mathbf{G}$  is a matrix created from Dirichlet boundary conditions such that  $\mathbf{G} \mathbf{u}_\theta^{p+1} = \mathbf{w}_0$ .

The extended system of Eq. (35) can now be solved for  $\mathbf{u}_\theta^{p+1}$  and  $\lambda$  at each time step. The solving process is iterated until the relative residual  $\mathbf{F}(\mathbf{u}_{\theta,z_1}^{p+1}, \dots, \mathbf{u}_{\theta,z_m}^{p+1})$  of  $m$  free nodes  $(z_1, \dots, z_m) \in \Xi$ , where  $\Xi$

is the set of free nodes, is smaller than a given tolerance or the maximum number of iterations is larger than a prescribed number.

### 2.6. Discretization in space using the FS-FEM

In the FS-FEM, the domain discretization is still based on the tetrahedral elements as in the standard FEM, but the basic stiffness matrix in the weak form (29) is performed based on the “smoothing domains” associated with the faces, and strain smoothing technique [3] is used. In such an integration process, the closed problem domain  $\Omega$  is divided into  $N_{sc} = N_f$  smoothing domains associated with faces such that  $\Omega = \sum_{k=1}^{N_f} \Omega^{(k)}$  and  $\Omega^{(i)} \cap \Omega^{(j)} = \emptyset, i \neq j$ , in which  $N_f$  is the total number of faces located in the entire problem domain. For tetrahedral elements, the smoothing domain  $\Omega^{(k)}$  associated with the face  $k$  is created by connecting three endpoints of the face to centroids of adjacent elements as shown in Fig. 4.

Using the face-based smoothing domains, smoothed strains  $\tilde{\epsilon}_k$  can now be obtained using the compatible strains  $\epsilon = \nabla_s \mathbf{u}_\theta$  through the following smoothing operation over domain  $\Omega^{(k)}$  associated with face  $k$

$$\tilde{\epsilon}_k = \int_{\Omega^{(k)}} \epsilon(\mathbf{x}) \Phi_k(\mathbf{x}) d\Omega = \int_{\Omega^{(k)}} \nabla_s \mathbf{u}_\theta(\mathbf{x}) \Phi_k(\mathbf{x}) d\Omega \quad (36)$$

where  $\Phi_k(\mathbf{x})$  is a given smoothing function that satisfies at least unity property

$$\int_{\Omega^{(k)}} \Phi_k(\mathbf{x}) d\Omega = 1 \quad (37)$$

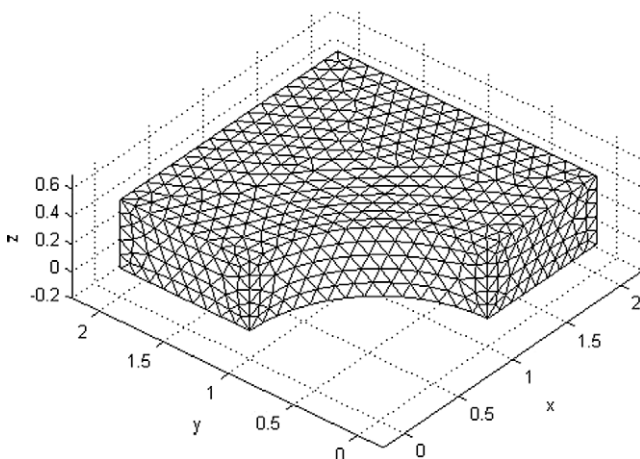


**Fig. 8.** A domain discretization using 2007 nodes and 8998 tetrahedral elements for the thick plate with a cylindrical hole subjected to time dependent surface forces  $g(t)$ .

**Table 1**  
Number of iterations and the estimated error using FEM and FS-FEM at various time steps for the thick plate with cylindrical hole.

Step	FEM		FS-FEM	
	Iterations	$\eta^h = \frac{\ \mathbf{R}^h - \sigma^h\ _{L_2}}{\ \sigma^h\ _{L_2}}$	Iterations	$\eta^h = \frac{\ \mathbf{R}^h - \sigma^h\ _{L_2}}{\ \sigma^h\ _{L_2}}$
1	1	0.1276	1	0.0877
2	1	0.1276	1	0.0877
3	1	0.1276	1	0.0877
4	1	0.1276	1	0.0877
5	1	0.1276	1	0.0877
6	1	0.1276	1	0.0877
7	1	0.1276	1	0.0877
8	4	0.1272	3	0.0874
9	4	0.1271	4	0.0870
10	4	0.1280	4	0.0872

In the FS-FEM [49], we use the simplest local constant smoothing function

$$\Phi_k(\mathbf{x}) = \begin{cases} 1/V^{(k)} & \mathbf{x} \in \Omega^{(k)} \\ 0 & \mathbf{x} \notin \Omega^{(k)} \end{cases} \quad (38)$$

where  $V^{(k)}$  is the volume of the smoothing domain  $\Omega^{(k)}$  and is calculated by

$$V^{(k)} = \int_{\Omega^{(k)}} d\Omega = \frac{1}{4} \sum_{j=1}^{N_e^{(k)}} V_e^{(j)} \quad (39)$$

where  $N_e^{(k)}$  is the number of elements attached to the face  $k$  ( $N_e^{(k)} = 1$  for the boundary faces and  $N_e^{(k)} = 2$  for inner faces) and  $V_e^{(j)}$  is the volume of the  $j^{th}$  element around the face  $k$ .

In the FS-FEM, the trial function used for each tetrahedral element is similar as in the standard FEM with

$$\mathbf{u}_{ij}^p = \sum_{i=1}^{3N_n} \varphi_i \mathbf{u}_i \quad (40)$$

Substituting Eqs. (40) and (38) into (36), the smoothed strain on the domain  $\Omega^{(k)}$  associated with face  $k$  can be written in the following matrix form of nodal displacements

$$\tilde{\boldsymbol{\varepsilon}}_k = \sum_{I \in \Psi_{df}^{(k)}} \tilde{\mathbf{B}}_I(\mathbf{x}_k) \mathbf{u}_I \quad (41)$$

where  $\Psi_{df}^{(k)}$  is the set containing degrees of freedom of elements attached to the face  $k$  (for example for the inner face  $k$  as shown in Fig. 4,  $\Psi_{df}^{(k)}$  is the set containing degrees of freedom of nodes  $\{A, B, C, D, E\}$  and the total number of degrees of freedom  $N_{df}^{(k)} = 15$ ) and  $\tilde{\mathbf{B}}_I(\mathbf{x}_k)$ , that is termed as the *smoothed strain matrix* on the domain  $\Omega^{(k)}$ , is calculated numerically by an assembly process similarly as in the FEM

$$\tilde{\mathbf{B}}_I(\mathbf{x}_k) = \frac{1}{V^{(k)}} \sum_{j=1}^{N_e^{(k)}} \frac{1}{4} V_e^{(j)} \mathbf{B}_j \quad (42)$$

where  $\mathbf{B}_j = \sum_{I \in S_j^e} \mathbf{B}_I(\mathbf{x})$  is the gradient matrix of shape functions of the  $j^{th}$  element attached to the face  $k$ . It is assembled from the gradient matrices of shape functions  $\mathbf{B}_I(\mathbf{x})$  (in the standard FEM) of nodes in the set  $S_j^e$  which contains four nodes of the  $j^{th}$  tetrahedral element. Matrix  $\mathbf{B}_I(\mathbf{x})$  for the node  $I$  in tetrahedral elements has the form of

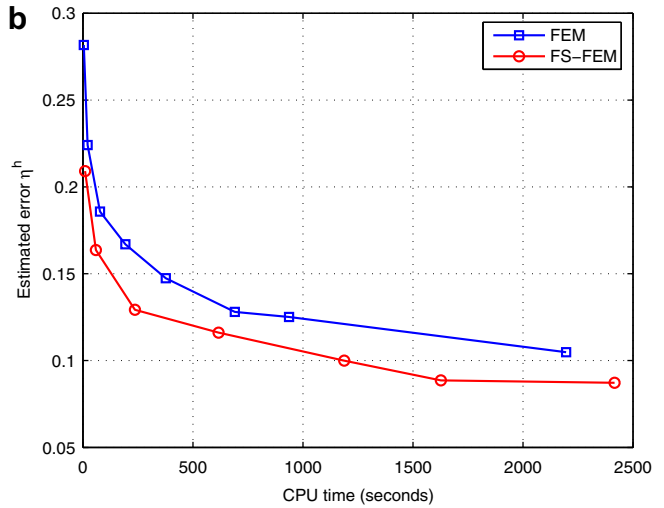
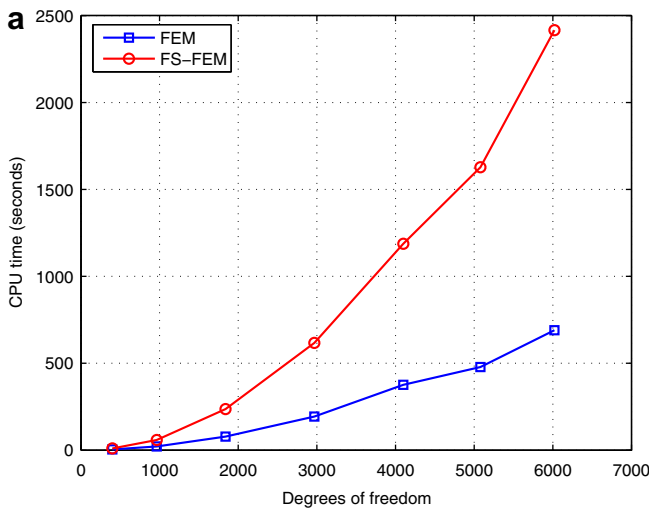


Fig. 9. Comparison of the computational cost and efficiency between FEM and FS-FEM for a range of meshes at  $t = 1$  for the thick plate with a cylindrical hole. (a) Computational cost; and (b) computational efficiency.

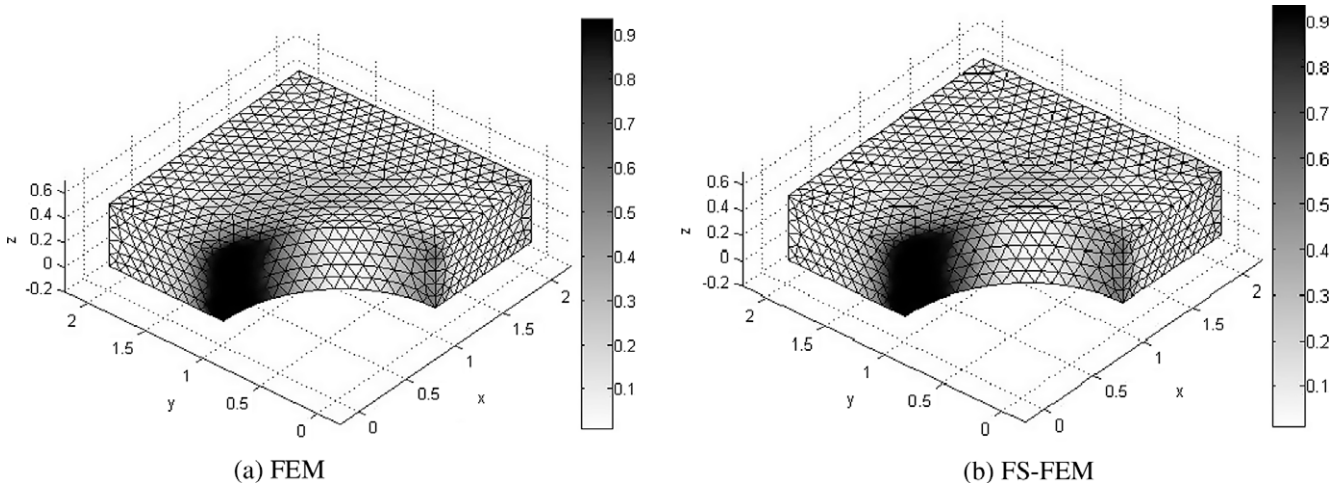
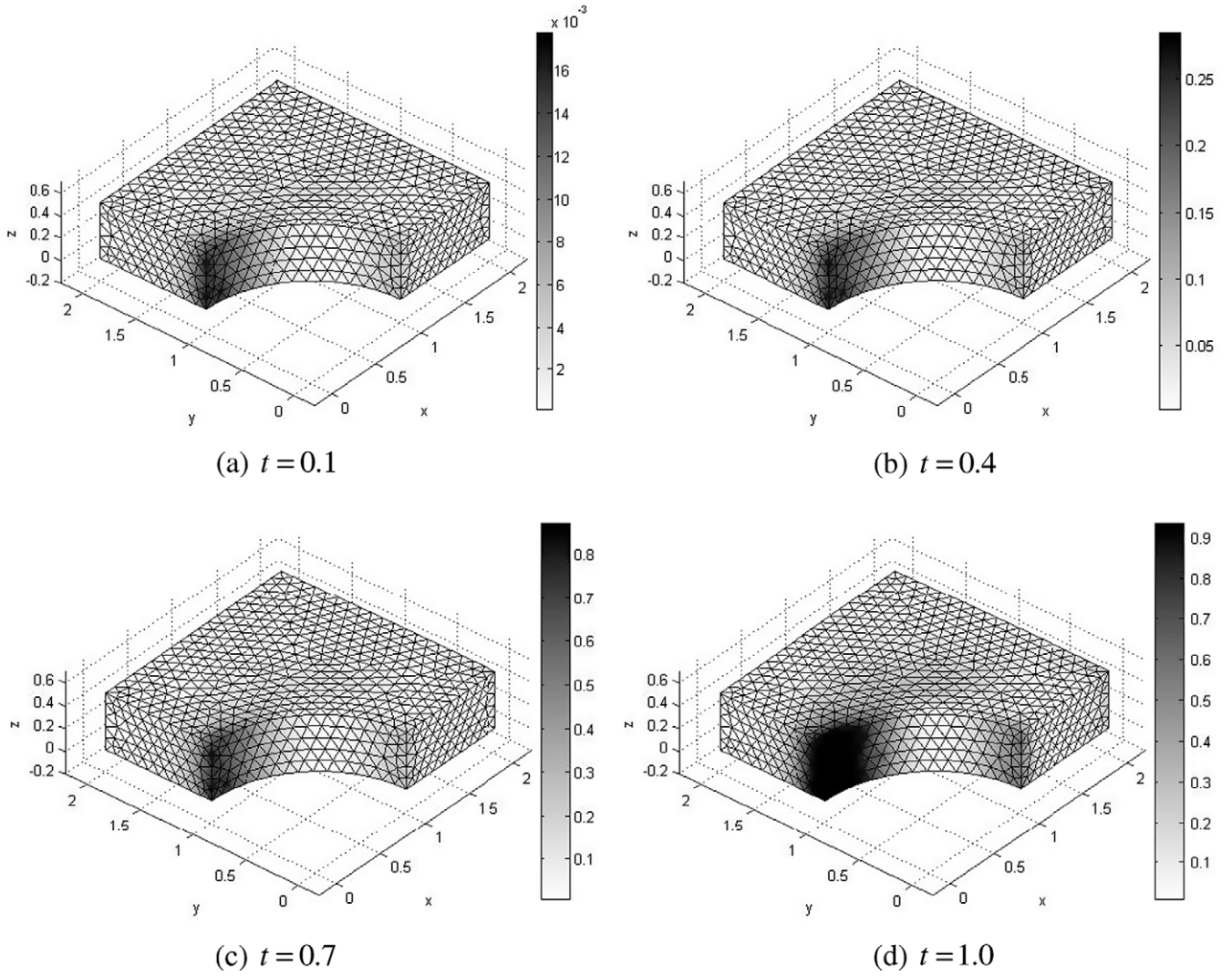
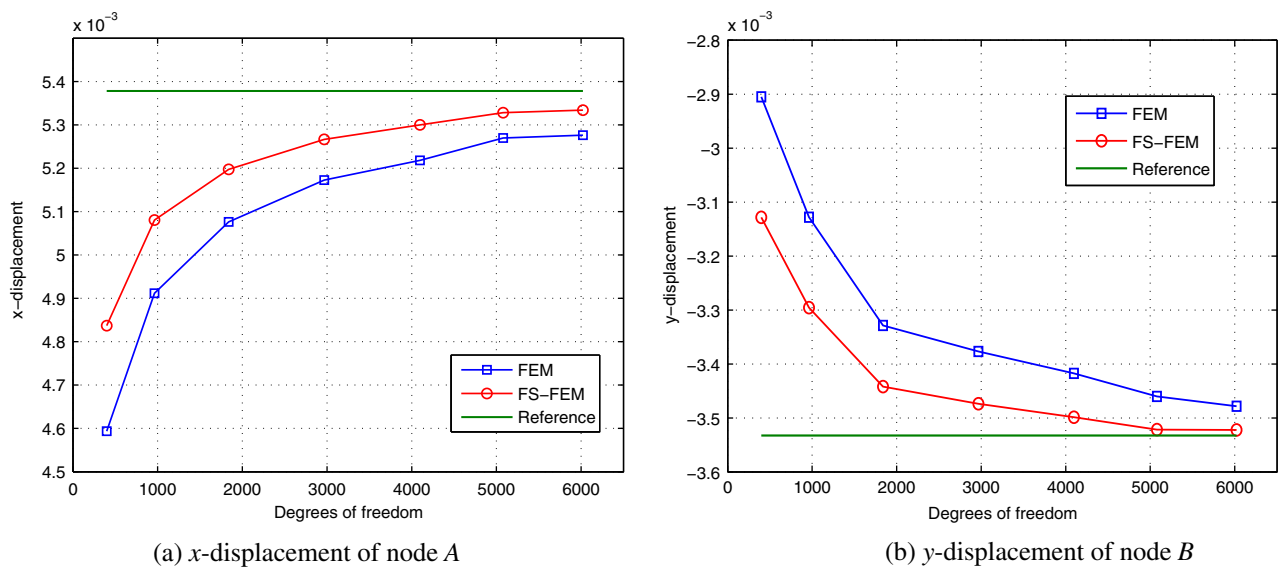


Fig. 10. Elastic shear energy density  $\|\text{div}(\mathbf{R}\boldsymbol{\sigma}^h)\|^2 / (4\mu)$  (the grey stone) of the plate with hole with cylindrical hole at  $t = 1.0$  (mesh with 2007 nodes and 8998 tetrahedral elements).



**Fig. 11.** Evolution of the elastic shear energy density  $\|\text{dev}(\mathbf{R}\sigma^h)\|^2/(4\mu)$  using FS-FEM at different time steps for the thick plate with cylindrical hole.



**Fig. 12.** Displacements at points A and B versus the number of degrees of freedom of the thick plate with cylindrical hole; (a) x-displacement of node A, (b) y-displacement of node B.

$$\mathbf{B}_I = \begin{bmatrix} \varphi_{1,x} & 0 & 0 \\ 0 & \varphi_{1,y} & 0 \\ 0 & 0 & \varphi_{1,z} \\ \varphi_{1,y} & \varphi_{1,x} & 0 \\ 0 & \varphi_{1,z} & \varphi_{1,y} \\ \varphi_{1,z} & 0 & \varphi_{1,x} \end{bmatrix} \quad (43)$$

Due to the use of the tetrahedral elements with the linear shape functions, the entries of matrix  $\mathbf{B}_j$  are constants, and so are the entries of matrix  $\tilde{\mathbf{B}}_j(\mathbf{x}_k)$ . Note that with this formulation, only the volume and the usual gradient matrices of shape functions  $\mathbf{B}_j$  of tetrahedral elements are needed to calculate the system stiffness matrix for the FS-FEM. One disadvantage of FS-FEM is that the bandwidth of stiffness matrix is larger than that of FEM, because the number of nodes related to the smoothing domains associated with inner faces is 5, which is 1 larger than that related to the elements. This is shown clearly by the set  $\Psi_{df}^{(k)} = \{A, B, C, D, E\}$  of the inner face  $k$  as shown in Fig. 4. The computational cost of FS-FEM therefore is larger than that of FEM for the same meshes.

In the discrete version of the visco-elastoplastic problems using the FS-FEM with the smoothed strain (36) used for smoothing domains associated with faces, the discrete problem Eq. (29) now becomes: seeking  $\mathbf{u}_\theta \in V^h$  such that  $\mathbf{u}_\theta = \mathbf{w}_0$  on  $\Gamma_D$  and

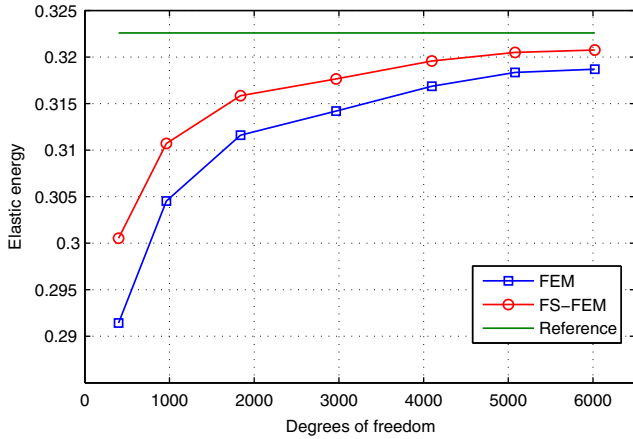


Fig. 13. Convergence of the elastic strain energy  $E = \int_{\Omega} \sigma_\theta : \epsilon_\theta d\Omega$  versus the number of degrees of freedom at  $t = 1$  of the thick plate with cylindrical hole.

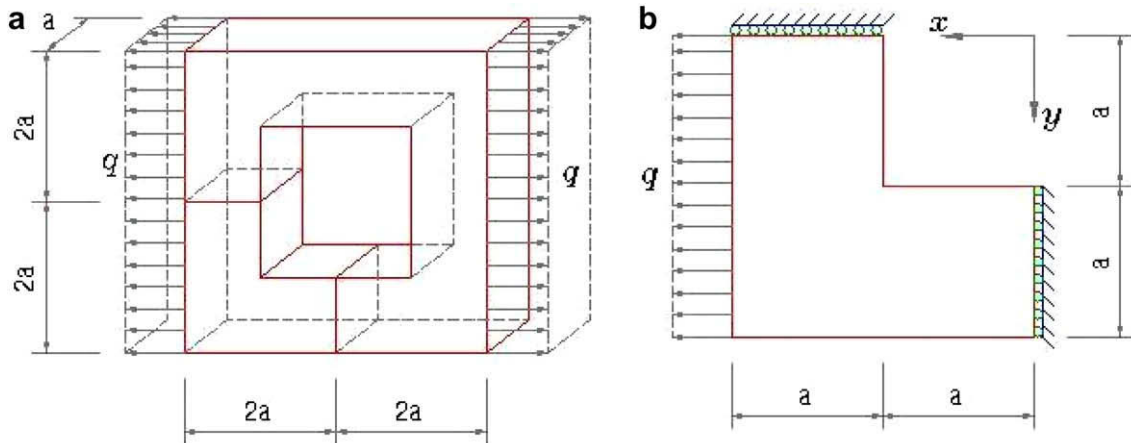


Fig. 14. (a) 3D square block with a cubic hole subjected to the surface traction  $q$ ; (b) 3D L-shaped problem modeled from an eighth of the 3D square block with a cubic hole (the length of long edge is  $2a$ , of the short edge is  $a$ , of thickness is  $a/2$  and symmetric conditions are imposed on the cutting boundary planes).

$$\begin{aligned} \mathbf{F}_i &= \int_{\Omega} \sigma_\theta (\tilde{\epsilon}(\mathbf{u}_\theta - \mathbf{u}_0) + \mathbf{C}^{-1} \sigma_0) \\ &: \tilde{\epsilon}(\varphi_i) d\Omega - \int_{\Omega} \mathbf{b}_\theta \cdot \varphi_i d\Omega - \int_{\Gamma_N} \bar{\mathbf{t}}_\theta \cdot \varphi_i d\Gamma = 0 \end{aligned} \quad (44)$$

for  $i = 1, \dots, 3N_n$ , and the local stiffness matrix  $\mathbf{DF}_{rs}^{(k)}$  in Eq. (34) associated with smoothing domain  $\Omega^{(k)}$  can be expressed as follows

$$\begin{aligned} \mathbf{DF}_{rs}^{(k)} &= \frac{\partial \mathbf{F}_r^{(k)}}{\partial \mathbf{u}_{\theta,s}^p} = \frac{\partial \mathbf{Q}_r^{(k)}}{\partial \mathbf{u}_{\theta,s}^p} \\ &= \frac{\partial}{\partial \mathbf{u}_{\theta,s}^p} \left( \int_{\Omega^{(k)}} \sigma_\theta \left( \tilde{\epsilon}_k \left( \sum_{l \in \Psi_{df}^{(k)}} \mathbf{u}_{\theta,l}^p \varphi_l - \mathbf{u}_0 \right) + \mathbf{C}^{-1} \sigma_0 \right) : \tilde{\epsilon}_k(\varphi_r) d\Omega \right) \end{aligned} \quad (45)$$

where  $r, s \in \Psi_{df}^{(k)}$ , and

$$\mathbf{Q}_r^{(k)} = \int_{\Omega^{(k)}} \sigma_\theta (\tilde{\epsilon}_k(\mathbf{u}_\theta - \mathbf{u}_0) + \mathbf{C}^{-1} \sigma_0) : \tilde{\epsilon}_k(\varphi_r) d\Omega \quad (46)$$

The expression  $\sigma_\theta (\tilde{\epsilon}_k(\mathbf{u}_\theta - \mathbf{u}_0) + \mathbf{C}^{-1} \sigma_0)$  in Eqs. (45) and (46) now is replaced by  $\sigma_\theta$  written explicitly in Eqs. 19, 20, 22, 23, 25, 26 for different cases of visco-elastoplasticity with just replacing  $\epsilon$  by  $\epsilon_k$  in corresponding positions which give the following results

(a) Perfect visco-elastoplasticity

$$\mathbf{Q}_r^{(k)} = V^{(k)} (C_1 \text{tr}(\tilde{\mathbf{v}}_k) \text{tr}(\tilde{\epsilon}_k(\varphi_r)) + C_4 \text{dev}(\tilde{\mathbf{v}}_k) : \tilde{\epsilon}_k(\varphi_r)) \quad (47)$$

$$\begin{aligned} \mathbf{DF}_{rs}^{(k)} &= V^{(k)} (C_1 \text{tr}(\tilde{\epsilon}_k(\varphi_r)) \text{tr}(\tilde{\epsilon}_k(\varphi_s)) + C_4 \text{dev}(\tilde{\epsilon}_k(\varphi_r)) : \tilde{\epsilon}_k(\varphi_s) \\ &- (C_5)_r \text{dev}(\tilde{\mathbf{v}}_k) : \tilde{\epsilon}_k(\varphi_s)) \end{aligned} \quad (48)$$

where  $\tilde{\mathbf{v}}_k = \tilde{\epsilon}_k(\mathbf{u}_\theta - \mathbf{u}_0) + \mathbf{C}^{-1} \sigma_0$  and

$$C_4 = \begin{cases} C_2 + C_3 / \|\text{dev}(\tilde{\mathbf{v}}_k)\| & \text{if } \|\text{dev}(\tilde{\mathbf{v}}_k)\| - \beta \sigma_Y > 0 \\ 2\mu & \text{else} \end{cases}$$

$$C_5 = \begin{cases} C_3 / \|\text{dev}(\tilde{\mathbf{v}}_k)\|^3 [\text{dev}(\tilde{\epsilon}_k(\varphi_r)) : \text{dev}(\tilde{\mathbf{v}}_k)]_{r=1}^{N_{df}^{(k)}} & \text{if } \|\text{dev}(\tilde{\mathbf{v}}_k)\| - \beta \sigma_Y > 0 \\ [0 \dots 0]^T & \text{else} \end{cases} \quad (49)$$

size of  $1 \times N_{df}^{(k)}$

in which  $C_1, C_2, C_3$  is determined by Eq. (21)

(b) Visco-elastoplasticity with isotropic hardening

$$\mathbf{Q}_r^{(k)} = V^{(k)} (C_1 \text{tr}(\tilde{\mathbf{v}}_k) \text{tr}(\tilde{\mathbf{e}}_k(\varphi_r) + C_5 \text{dev}(\tilde{\mathbf{v}}_k) : \tilde{\mathbf{e}}_k(\varphi_r)) \quad (50)$$

$$\mathbf{DF}_{rs}^{(k)} = V^{(k)} (C_1 \text{tr}(\tilde{\mathbf{e}}_k(\varphi_r)) \text{tr}(\tilde{\mathbf{e}}_k(\varphi_s)) + C_5 \text{dev}(\tilde{\mathbf{e}}_k(\varphi_r)) : \tilde{\mathbf{e}}_k(\varphi_s) - (C_6)_r \text{dev}(\tilde{\mathbf{v}}_k) : \tilde{\mathbf{e}}_k(\varphi_s)) \quad (51)$$

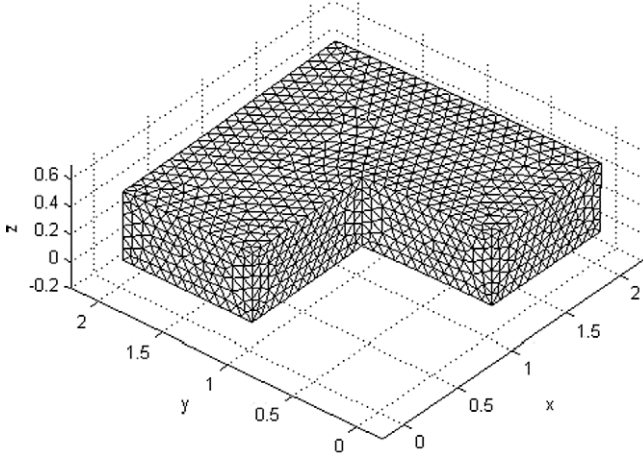


Fig. 15. A domain discretization using 2327 nodes and 10584 tetrahedral elements for the 3D L-shaped problem.

Table 2  
Number of iterations and the estimated error using FEM and FS-FEM at various time steps for the 3D L-shaped problem.

Step	FEM		FS-FEM	
	Iterations	$\eta^h = \frac{\ \mathbf{R}\sigma^h - \sigma^h\ _{L_2}}{\ \sigma^h\ _{L_2}}$	Iterations	$\eta^h = \frac{\ \mathbf{b}\mathbf{R}\sigma^h - \sigma^h\ _{L_2}}{\ \sigma^h\ _{L_2}}$
1	1	0.1343	1	0.0951
2	1	0.1343	1	0.0951
3	1	0.1343	1	0.0951
4	1	0.1343	1	0.0951
5	2	0.1343	2	0.0951
6	3	0.1344	3	0.0952
7	4	0.1351	4	0.0955
8	4	0.1358	4	0.0953
9	4	0.1365	4	0.0949
10	5	0.1385	5	0.0950

where

$$C_5 = \begin{cases} C_3 / (C_2 \|\text{dev}(\tilde{\mathbf{v}}_k)\|) + C_4 / C_2 & \text{if } \|\text{dev}(\tilde{\mathbf{v}}_k)\| - \beta(1 + \alpha_0^l H) \sigma_Y > 0 \\ 2\mu & \text{else} \end{cases}$$

$$C_6 = \begin{cases} C_3 / (C_2 \|\text{dev}(\tilde{\mathbf{v}}_k)\|^3) [\text{dev}(\tilde{\mathbf{e}}_k(\varphi_r)) : \text{dev}(\tilde{\mathbf{v}}_k)]_{r=1}^{N_{df}^{(k)}} & \text{if } \|\text{dev}(\tilde{\mathbf{v}}_k)\| - \beta(1 + \alpha_0^l H) \sigma_Y > 0 \\ [0 \dots 0]^T & \text{else} \end{cases} \quad (52)$$

size of  $1 \times N_{df}^{(k)}$

in which  $C_1, C_2, C_3, C_4$  is determined by Eq. (24)

(c) Visco-elastoplasticity with linear kinematic hardening

$$\mathbf{Q}_r^{(k)} = V^{(k)} (C_1 \text{tr}(\tilde{\mathbf{v}}_k) \text{tr}(\tilde{\mathbf{e}}_k(\varphi_r)) + C_4 \text{dev}(\tilde{\mathbf{v}}_k) : \tilde{\mathbf{e}}_k(\varphi_r) + c \text{dev}(\alpha_0^K) : \tilde{\mathbf{e}}_k(\varphi_r)) \quad (53)$$

$$\mathbf{DF}_{rs}^{(k)} = V^{(k)} (C_1 \text{tr}(\tilde{\mathbf{e}}_k(\varphi_r)) \text{tr}(\tilde{\mathbf{e}}_k(\varphi_s)) + C_4 \text{dev}(\tilde{\mathbf{e}}_k(\varphi_r)) : \tilde{\mathbf{e}}_k(\varphi_s) - (C_5)_r \text{dev}(\tilde{\mathbf{v}}_k) : \tilde{\mathbf{e}}_k(\varphi_s)) \quad (54)$$

where

$$C_4 = \begin{cases} C_3 / \|\text{dev}(\tilde{\mathbf{v}}_k)\| + C_2 & \text{if } \|\text{dev}(\tilde{\mathbf{v}}_k - \beta \alpha_0^K)\| - \beta \sigma_Y > 0 \\ 2\mu & \text{else} \end{cases}$$

$$C_5 = \begin{cases} C_3 / \|\text{dev}(\tilde{\mathbf{v}}_k)\|^3 [\text{dev}(\tilde{\mathbf{e}}_k(\varphi_r)) : \text{dev}(\tilde{\mathbf{v}}_k)]_{r=1}^{N_{df}^{(k)}} & \text{if } \|\text{dev}(\tilde{\mathbf{v}}_k - \beta \alpha_0^K)\| - \beta \sigma_Y > 0 \\ [0 \dots 0]^T & \text{else} \end{cases} \quad (55)$$

size of  $1 \times N_{df}^{(k)}$

$$c = \begin{cases} 1 & \text{if } \|\text{dev}(\tilde{\mathbf{v}}_k - \beta \alpha_0^K)\| - \beta \sigma_Y > 0 \\ 0 & \text{else} \end{cases}$$

in which  $C_1, C_2, C_3$  is determined by Eq. (27)

Applying the Dirichlet boundary conditions and solving the extended system of Eq. (35) by the FS-FEM are identical to those of the FEM.

We also note that the trial function  $\mathbf{u}_y(\mathbf{x})$  for elements in the FS-FEM is the same as in the standard FEM and therefore the force

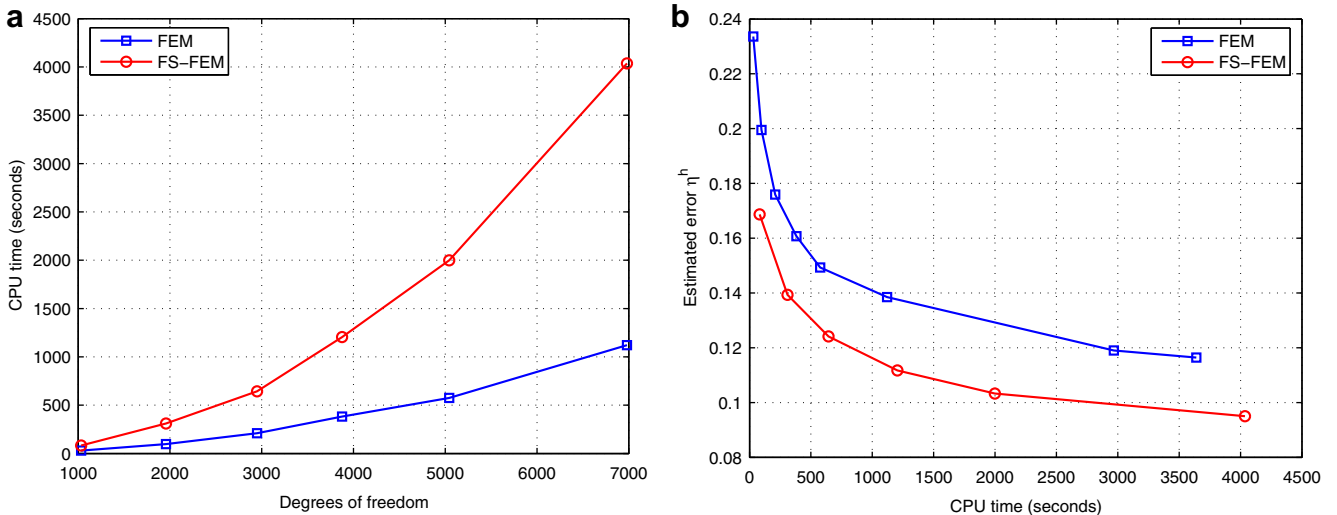


Fig. 16. Comparison of the computational cost and efficiency between FEM and FS-FEM for a range of meshes at  $t = 1$  for the 3D L-shaped problem. (a) Computational cost; and (b) computational efficiency.

vector  $\mathbf{P}_i$  in the FS-FEM is computed in the same way as in the FEM. In other words, the FS-FEM changes only the stiffness matrix. Figs. 5 and 6 present the flow chart to solve the visco-elastoplastic problems using the FS-FEM.

### 3. A posteriori error estimator

In order to estimate the accuracy of FS-FEM compared to FEM for the visco-elastoplastic problems, in this work we will use the

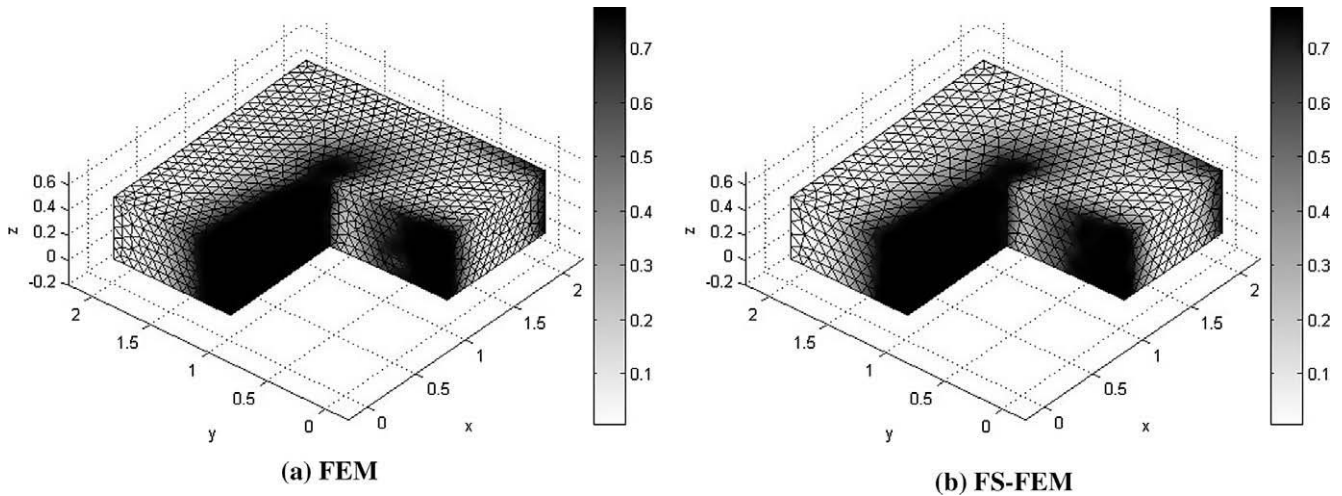


Fig. 17. Elastic shear energy density  $\|\text{dev}(\mathbf{R}\sigma^h)\|^2/(4\mu)$  (the grey stone) of the 3D L-shaped problem at  $t = 1.0$  (mesh with 2327 nodes and 10,584 tetrahedral elements).

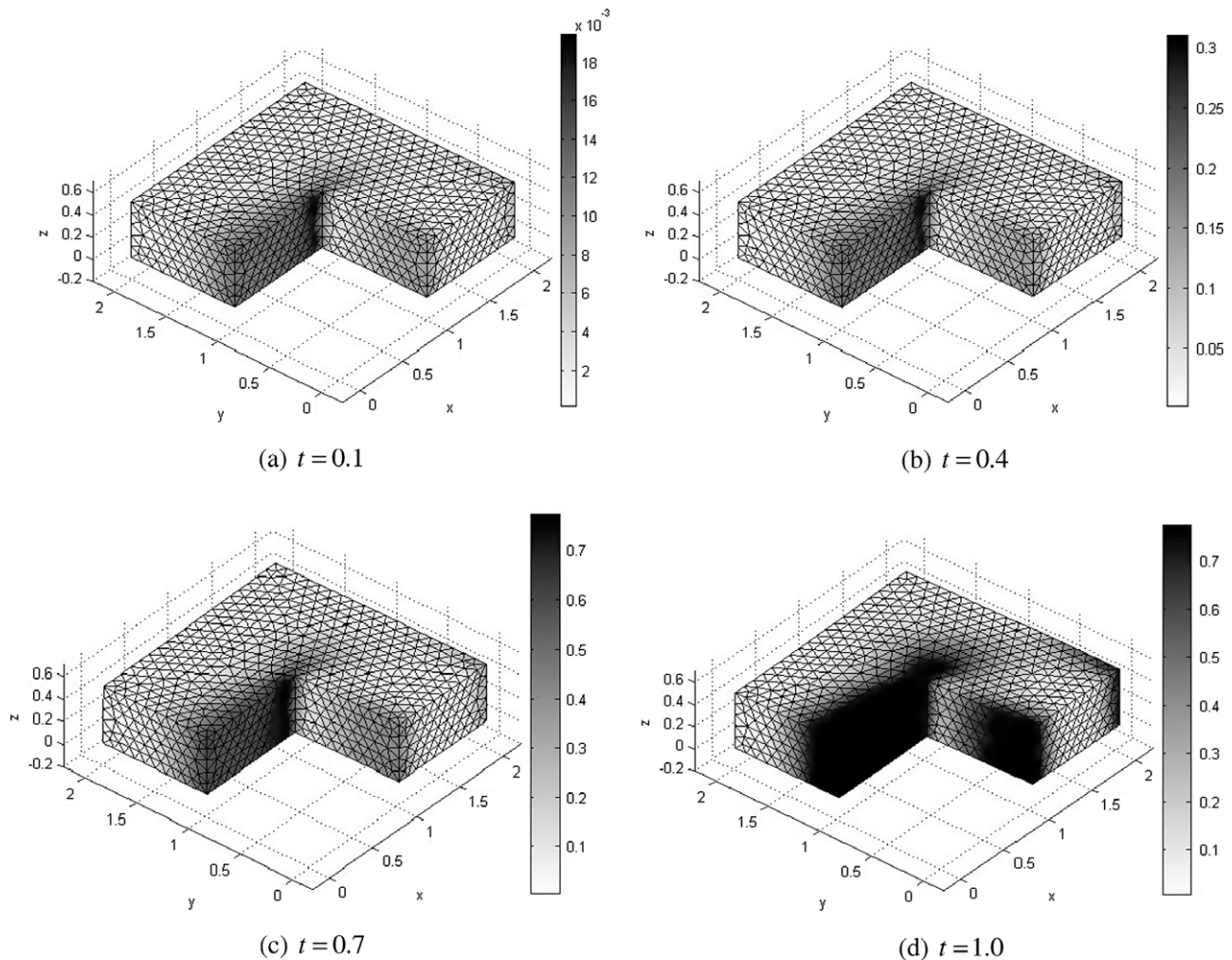


Fig. 18. Evolution of the elastic shear energy density  $\|\text{dev}(\mathbf{R}\sigma^h)\|^2/(4\mu)$  using FS-FEM at different time steps for the 3D L-shaped problem.

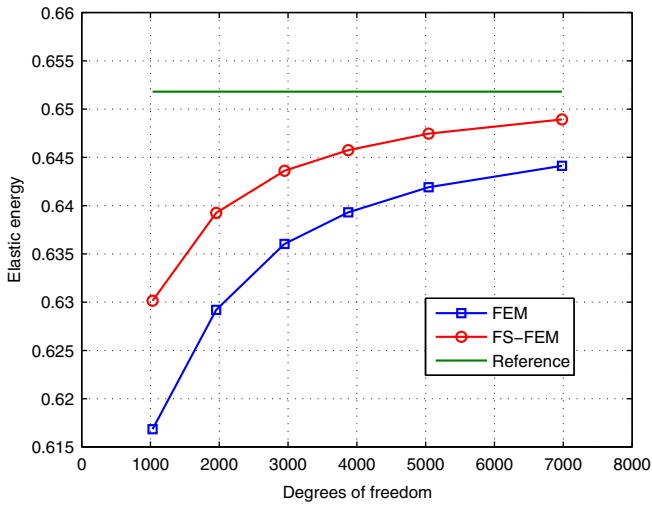


Fig. 19. Convergence of the elastic strain energy  $E = \int_{\Omega} \sigma_n : \epsilon_n d\Omega$  versus the number of degrees of freedom at  $t = 1$  of the 3D L-shaped problem.

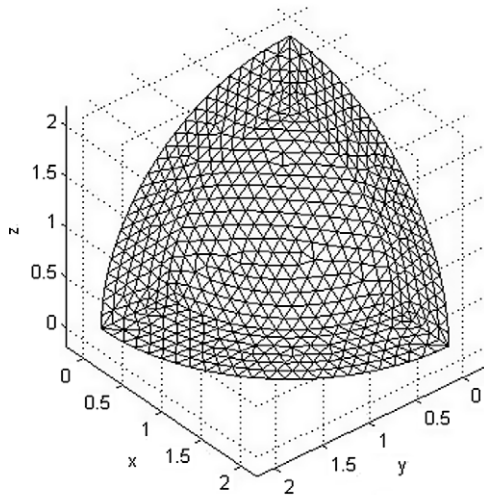


Fig. 20. A eighth of the hollow sphere discretized by 2234 nodes and 10,385 tetrahedral elements.

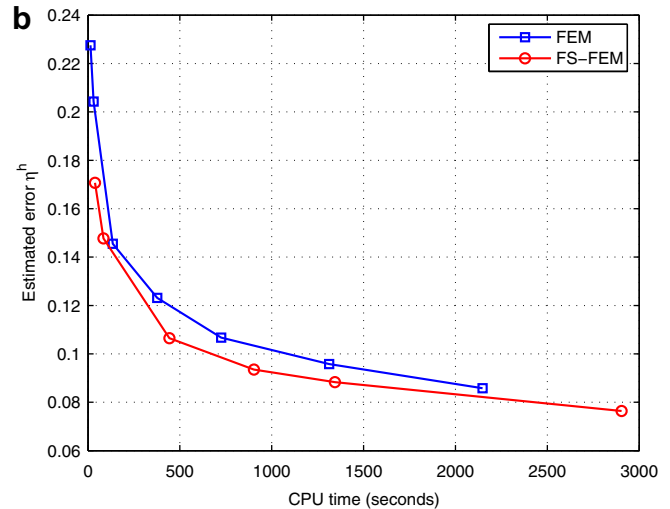
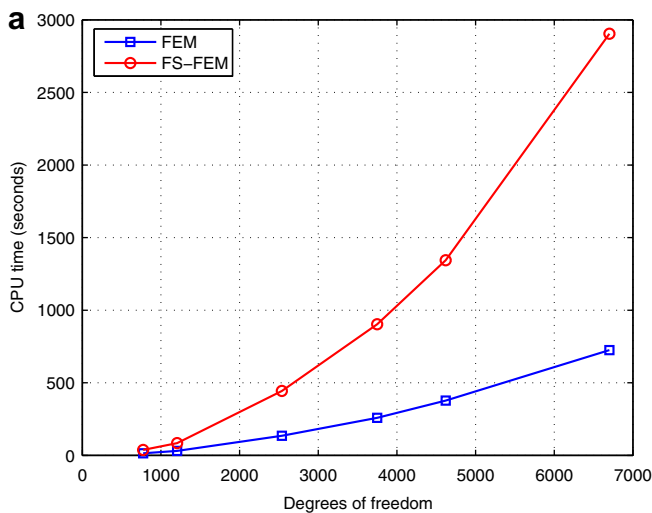


Fig. 21. Comparison of the computational cost and efficiency between FEM and FS-FEM for a range of meshes at  $t = 1$  for the hollow sphere problem. (a) Computational cost; and (b) computational efficiency.

Table 3

Number of iterations and the estimated error using FEM and FS-FEM at various time steps for hollow sphere problem.

Step	FEM		FS-FEM	
	Iterations	$\eta^h = \frac{\ \mathbf{R}\sigma^h - \sigma^h\ _{L_2}}{\ \sigma^h\ _{L_2}}$	Iterations	$\eta^h = \frac{\ b/R\sigma^h - \sigma^h\ _{L_2}}{\ \sigma^h\ _{L_2}}$
1	1	0.1067	1	0.0766
2	1	0.1067	1	0.0766
3	1	0.1067	1	0.0766
4	1	0.1067	1	0.0766
5	1	0.1067	1	0.0766
6	1	0.1067	1	0.0766
7	1	0.1067	1	0.0766
8	2	0.1067	2	0.0766
9	3	0.1067	3	0.0765
10	3	0.1067	3	0.0764

following efficient a posteriori error [50–57] which was verified as an error estimator in Refs. [24,50]

$$\eta^h = \frac{\|\mathbf{R}\sigma^h - \sigma^h\|_{L_2(\Omega)}}{\|\sigma^h\|_{L_2(\Omega)}} = \frac{\left(\sum_{e=1}^{N_e} \int_{\Omega_e} (\mathbf{R}\sigma^h - \sigma^h) : (\mathbf{R}\sigma^h - \sigma^h) d\Omega\right)^{1/2}}{\left(\sum_{e=1}^{N_e} \int_{\Omega_e} \sigma^h : \sigma^h d\Omega\right)^{1/2}} \quad (56)$$

where  $\mathbf{R}\sigma^h$  is a globally continuous recovery stress field derived from the discrete (discontinuous) numerical element stress field  $\sigma^h$ . The quantity  $\eta^h$  can monitor the local spatial approximation error, and a larger value of  $\eta^h$  implies a larger spatial error.

For the FS-FEM, when computing the stresses  $\sigma^h$  for an element, we can average the stresses of 4 smoothing domains associated with that element and the averaged stresses are regarded as the stresses of the element. Similarly, to calculate numerical stresses  $\sigma^h(\mathbf{x}_j)$  at a node  $\mathbf{x}_j$ , we simply average the stresses of all smoothing domains associated with the node. For the FEM, we can regard the stresses at the centroid as the element stresses  $\sigma^h$ , while the stresses  $\sigma^h(\mathbf{x}_j)$  at a node  $\mathbf{x}_j$  are the averaged stresses of those of the elements surrounding the node.

The recovery stress field  $\mathbf{R}\sigma^h$  in Eq. (56) for each element in the FS-FEM and the FEM now can be derived from the numerical stresses  $\sigma^h(\mathbf{x}_j)$  at the node  $\mathbf{x}_j$  by using the following approximation

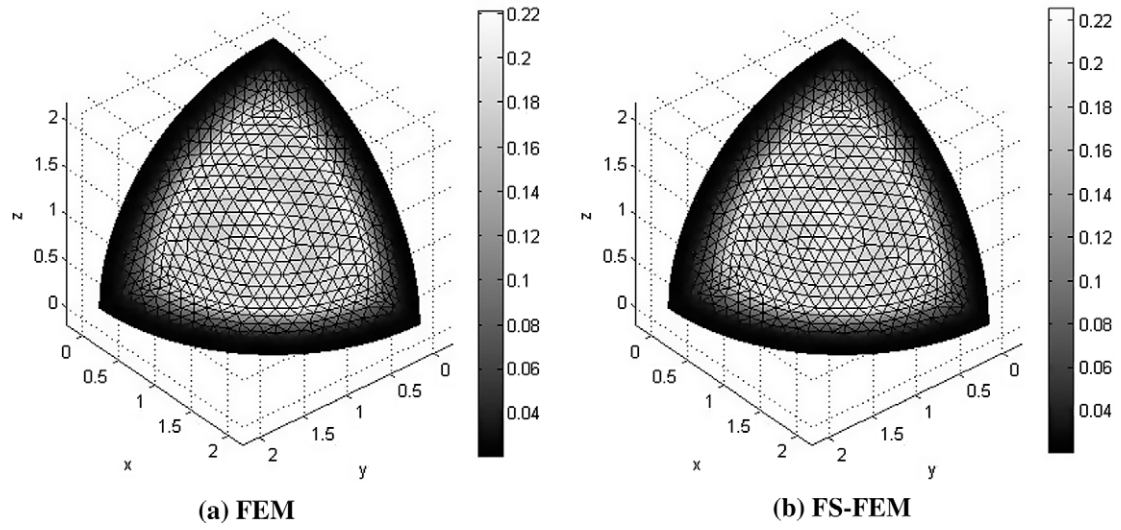


Fig. 22. Elastic shear energy density  $\|\text{dev}(\mathbf{R}\sigma^h)\|^2/(4\mu)$  for the hollow sphere problem using FEM and FS-FEM at  $t = 1.0$  (mesh with 2234 nodes and 10,385 elements).

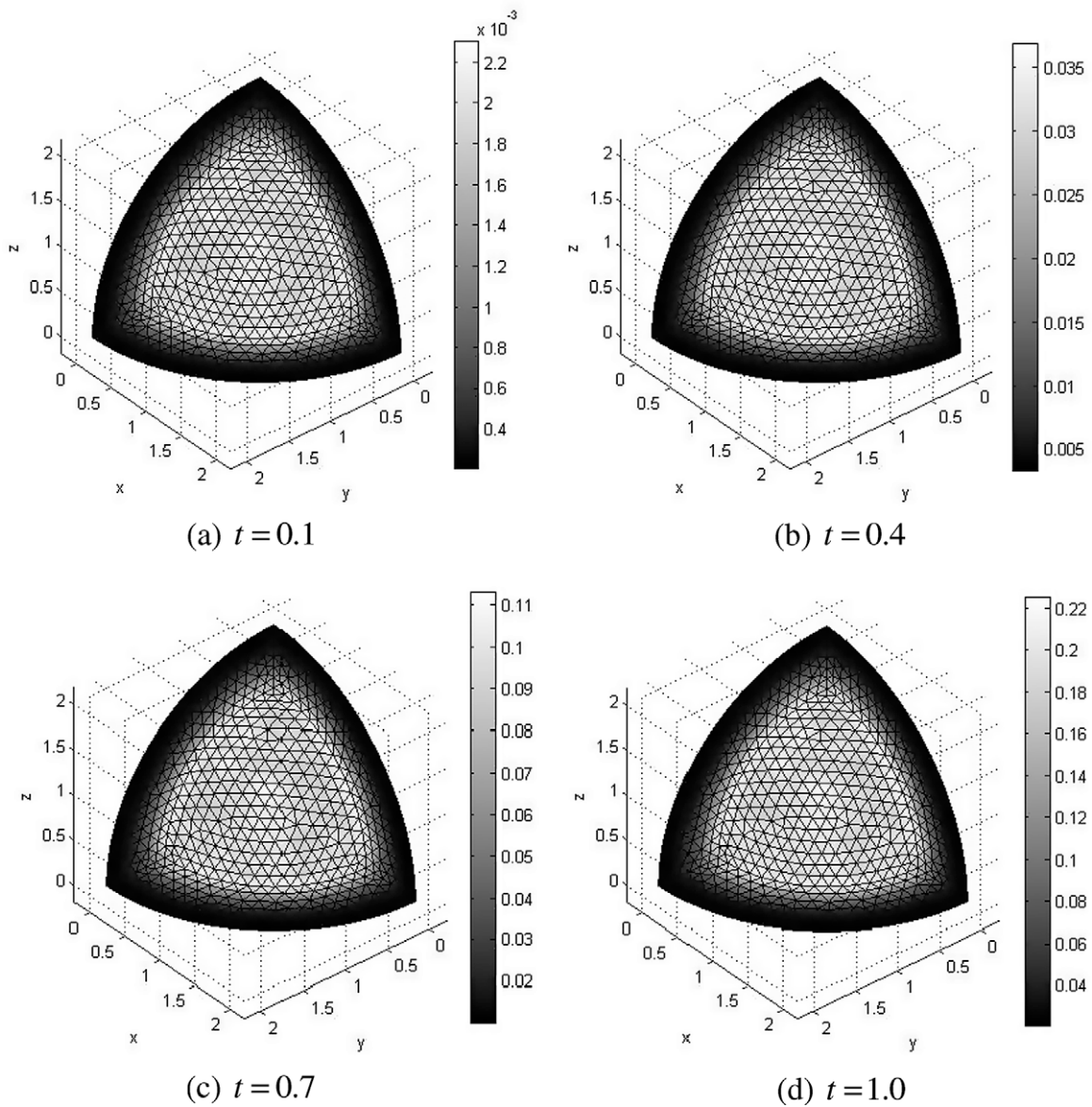


Fig. 23. Evolution of the elastic shear energy density  $\|\text{dev}(\mathbf{R}\sigma^h)\|^2/(4\mu)$  using FS-FEM at some different time steps for the hollow sphere problem.

**Table 4**

Radial displacements at points A(1.3,0,0) and B(0,1.3,0) using FEM and FS-FEM at various time steps of the hollow sphere problem.

Step	FEM			FS-FEM		
	$u_A$	$u_B$	$ u_A - u_B $	$u_A$	$u_B$	$ u_A - u_B $
1	0.0001664	0.0001658	6.45119E-07	0.0001682	0.0001680	1.87086E-07
2	0.0003328	0.0003315	1.29024E-06	0.0003364	0.0003364	0
3	0.0004992	0.0004973	1.93536E-06	0.0005046	0.0005040	5.61257E-07
4	0.0006656	0.0006630	2.58047E-06	0.0006728	0.0006720	7.48343E-07
5	0.0008320	0.0008288	3.22559E-06	0.0008410	0.0008400	9.35429E-07
6	0.0009984	0.0009945	3.87071E-06	0.0010092	0.0010081	1.12251E-06
7	0.0011648	0.0011603	4.51583E-06	0.0011774	0.0011761	1.3096E-06
8	0.0013312	0.0013260	5.15844E-06	0.0013456	0.0013441	1.49466E-06
9	0.0014980	0.0014922	5.80887E-06	0.0015142	0.00151251	1.6819E-06
10	0.0016667	0.0016603	6.46026E-06	0.0016850	0.00168311	1.84285E-06

$$\mathbf{R}\sigma^h = \sum_{j=1}^4 \mathbf{N}_j(\mathbf{x})\sigma^h(\mathbf{x}_j) \tag{57}$$

where  $\mathbf{N}_j(\mathbf{x})$  are the linear shape functions of tetrahedral elements used in the standard FEM, and  $\sigma^h(\mathbf{x}_j)$  are stress values at four nodes of the element.

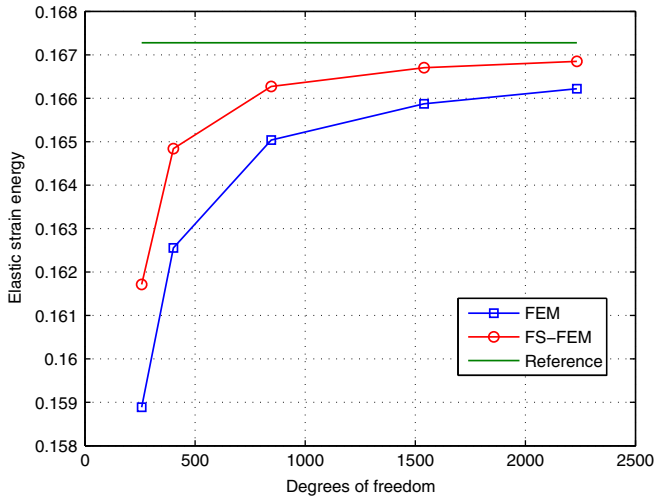


**Fig. 24.** Convergence of the elastic strain energy  $E = \int_{\Omega} \sigma_{ij} : \epsilon_{ij} d\Omega$  versus the number of degrees of freedom at  $t = 1$  of the hollow sphere problem.

In order to evaluate the integrals in Eq. (56) for tetrahedral elements, the mapping procedure using Gauss integration is performed on each element with a summation on all elements. In each element, a proper number of Gauss points depending on the order of the recovery solution  $\mathbf{R}\sigma^h$  will be used.

**4. Numerical examples**

In this section, four numerical examples are performed to demonstrate the properties of FS-FEM for three different visco-elastoplastic cases: perfect visco-elastoplasticity, visco-elastoplasticity with isotropic hardening and visco-elastoplasticity with linear kinematic hardening. To emphasize the advantages of the present method, the results of FS-FEM will be compared to those of Carstensen and Klose [50] using the standard FEM.

**4.1. A thick plate with a cylindrical hole: perfect visco-elastoplasticity**

Fig. 7 represents a thick plate  $\Omega$  with the dimensions in  $xOy$  plane as  $[-2,2] \times [-2,2]$  and the thickness in  $z$  direction as  $[-0.5,0.5]$ . The plate has a central cylindrical hole in  $z$ -direction with radius  $a = 1$  and is subjected to time dependent outer pressures  $g(t) = 100t$  in  $y$ -direction at two outer surfaces. Because of its symmetry, only the upper right octant of the plate is modeled. Symmetric conditions are imposed on cutting plane surfaces, and the inner boundary of the hole is traction free. Fig. 8 gives a discretization of the domain using 2007 nodes (6021 degrees of

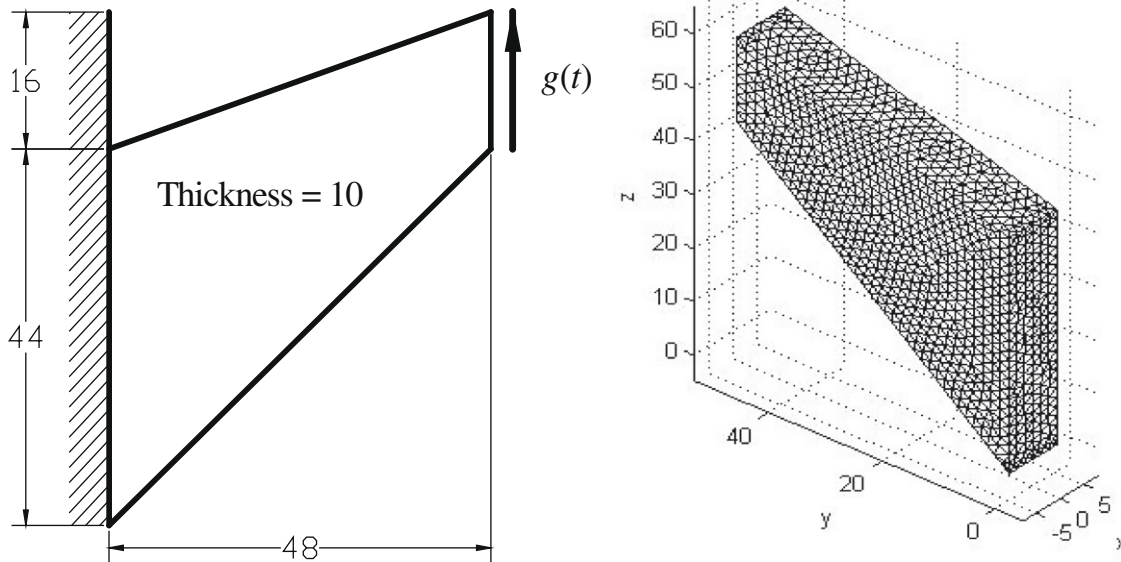


**Fig. 25.** The 3D Cook's membrane subjected to a time dependent shear force and its discretization using 2317 nodes and 9583 tetrahedral elements.

**Table 5**  
Number of iterations and the estimated error using FEM and FS-FEM at various time steps for the 3D Cook's membrane problem.

Step	FEM		FS-FEM	
	Iterations	$\eta^h = \frac{\ \mathbf{R}\sigma^h - \sigma^h\ _{L_2}}{\ \sigma^h\ _{L_2}}$	Iterations	$\eta^h = \frac{\ \mathbf{R}\sigma^h - \sigma^h\ _{L_2}}{\ \sigma^h\ _{L_2}}$
1	1	0.1101	1	0.0756
2	1	0.1101	1	0.0756
3	1	0.1101	1	0.0756
4	1	0.1101	1	0.0756
5	1	0.1101	1	0.0756
6	3	0.1101	3	0.0756
7	3	0.1101	3	0.0756
8	3	0.1106	4	0.0758
9	4	0.1115	4	0.0765
10	4	0.1130	4	0.0774

freedom) and 8998 tetrahedral elements. Assuming that the material is perfect visco-elastoplasticity with Young's modulus  $E = 206,900$ , Poisson's ratio  $\nu = 0.29$ , yield stress  $\sigma_Y = 550$ , and the initial data for the stress vector  $\sigma_0$  is set zero.

The solution is calculated in the time interval from  $t = 0$  to  $t = 1.0$  in 10 uniform steps  $\Delta t = 0.1$ . Using the mesh as shown in Fig. 8, the material remains elastic in seven first steps, between  $t = 0$  and  $t = 0.7$  for both the FS-FEM and FEM as shown in Table 1. Table 1 also shows that the number of iterations in Newton's method of both FS-FEM and FEM are almost the same, but the estimated errors  $\eta^h$  in Eq. (56) of FS-FEM are about 30% less than those of FEM. In addition, Fig. 9 compares the computational cost and efficiency between the FEM and FS-FEM for a range of meshes at  $t = 1$ . It is seen that with the same mesh, the computational cost of FS-FEM is larger than that of FEM as shown in Fig. 9a. However, when the efficiency of computation (computation time for the same accuracy) in terms of the error estimator versus computational cost for a range of meshes is considered, the FS-FEM is more efficient than the FEM as shown in Fig. 9b.

Fig. 10 shows the elastic shear energy density  $\|\text{dev}(\mathbf{R}\sigma^h)\|^2/(4\mu)$  at  $t = 1.0$  which is almost the same for FEM and FS-FEM generally. The evolution of the elastic shear energy density  $\|\text{dev}(\mathbf{R}\sigma^h)\|^2/(4\mu)$  is demonstrated using the FS-FEM at four different time instances as shown in Fig. 11 in which the plasticity domain first appears at

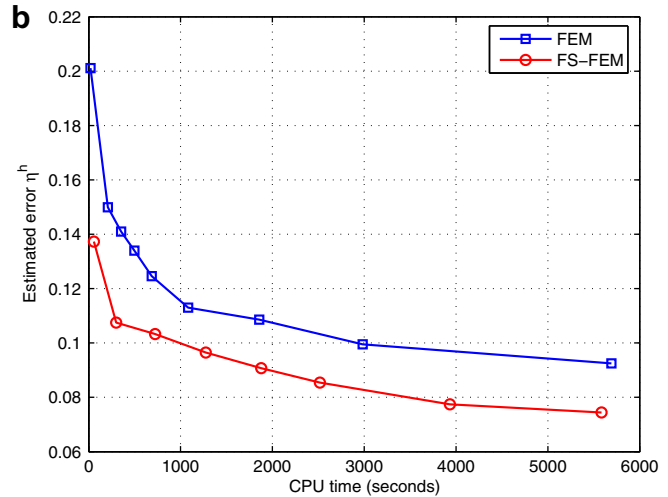
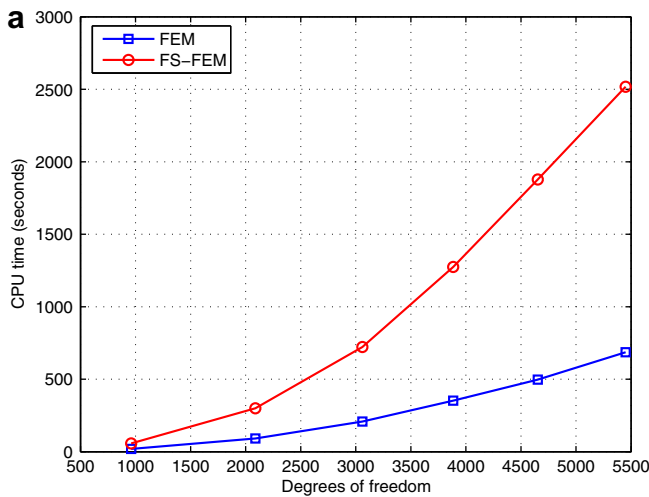


**Fig. 26.** Comparison of the computational cost and efficiency between FEM and FS-FEM for a range of meshes at  $t = 1$  for the 3D Cook's membrane problem. (a) Computational cost; and (b) computational efficiency.

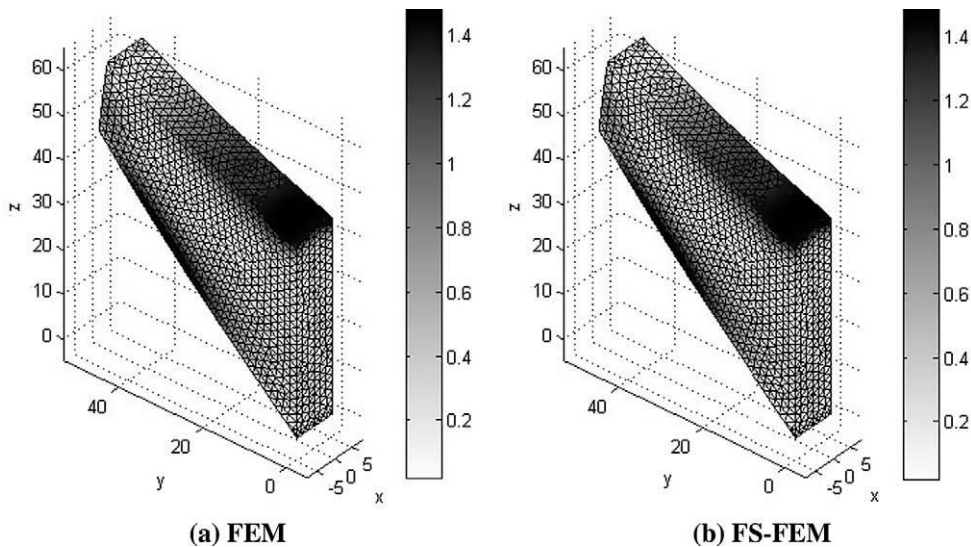


**Fig. 27.** Elastic shear energy density  $\|\text{dev}(b\mathbf{R}\sigma^h)\|^2/(4\mu)$  for 3D Cook's membrane problem using FEM and FS-FEM at  $t = 1.0$  (mesh with 2317 nodes and 9583 tetrahedral elements).



FS-FEM is larger than that of FEM as shown in Fig. 16a. However, when the efficiency of computation (computation time for the same accuracy) in terms of the error estimator versus computational cost for a range of meshes is considered, the FS-FEM is more efficient than the FEM as shown in Fig. 16b.

Fig. 17 shows the elastic shear energy density  $\|\text{dev}(\mathbf{R}\sigma^h)\|^2/(4\mu)$  at  $t = 1.0$  which is also almost the same for the FEM and FS-FEM. The evolution of the elastic shear energy density  $\|\text{dev}(\mathbf{R}\sigma^h)\|^2/(4\mu)$  is demonstrated using the FS-FEM at four different time instances as shown in Fig. 18 in which the plastic domain first appears at the re-entrant corner.

Fig. 19 shows the convergence of the elastic strain energy  $E = \int_{\Omega} \sigma_{ij} : \epsilon_{ij} d\Omega$  versus the number of degrees of freedom using the FEM and FS-FEM at  $t = 1.0$ . The solution of FS-FEM using a very fine mesh including 15,390 degrees of freedom and 24,777 elements is used as reference solution. The results again verify that the FS-FEM model is softer and gives more accurate results than the FEM model using tetrahedral elements.

4.3. The hollow sphere problem: visco-elastoplasticity with isotropic hardening

The domain is the hollow sphere  $\Omega = B(0, 2) \setminus B(0, 1.3)$  (the origin  $O(0, 0, 0)$ , inner radius  $a = 1.3$ , outer radius  $b = 2.0$ ) subjected to a uniform pressure  $g(r, \varphi, t) = 50te_r$  on inner radius with  $e_r = (\cos \varphi, \sin \varphi)$ . Because of the symmetric characteristic of the problem, only a eighth of hollow sphere is modeled as shown in Fig. 20, and symmetric conditions are imposed on the cutting boundary planes. Assuming that the material is visco-elastoplasticity with isotropic hardening with Young's modulus  $E = 40,000$ , Poisson's ratio  $\nu = 0.25$ , yield stress  $\sigma_Y = 100$ , hardening parameter  $H = 3, H_1 = 1$ ; and the initial stress vector  $\sigma_0$  and the scalar hardening parameter  $\alpha_0^k$  are set zero.

The solution is calculated in the time interval from  $t = 0$  to  $t = 1.0$  in 10 uniform steps  $\Delta t = 0.1$ . Using the mesh as shown in Fig. 20, the material remains elastic in seven first steps, between  $t = 0$  and  $t = 0.7$  for both the FS-FEM and FEM as shown in Table 3. Table 3 also shows that the number of iterations in Newton's method of both FS-FEM and FEM are almost the same, but the estimated errors  $\eta^h$  in Eq. (56) of FS-FEM are about 30% less than those of FEM. In addition, Fig. 21 compares the computational cost and efficiency between the FEM and FS-FEM for a range of meshes at  $t = 1$ . It is seen that with the same mesh, the computational cost of FS-FEM is larger than that of FEM as shown in Fig. 21a. However, when the efficiency of computation (computation time for the same accuracy) in terms of the error estimator versus computational cost for a range of meshes is considered, the FS-FEM is more efficient than the FEM as shown in Fig. 21b.

Fig. 22 shows the elastic shear energy density  $\|\text{dev}(\mathbf{R}\sigma^h)\|^2/(4\mu)$  at  $t = 1.0$  which is also almost the same for the FEM and FS-FEM. The evolution of the elastic shear energy density  $\|\text{dev}(\mathbf{R}\sigma^h)\|^2/(4\mu)$  is demonstrated using the FS-FEM at some different time instances as shown in Fig. 23 in which the plastic domain first appears at the inner radius and extends toward the outer radius. Table 4 shows the ratio of radial displacements between points  $A(1.3, 0, 0)$  and  $B(0, 1.3, 0)$  using the FEM and FS-FEM at various time steps. It is seen that for the symmetric problem, the results of FS-FEM is more symmetric than those of FEM.

Fig. 24 shows the convergence of the elastic strain energy  $E = \int_{\Omega} \sigma_{ij} : \epsilon_{ij} d\Omega$  versus the number of degrees of freedom using the FEM and FS-FEM at  $t = 1.0$ . The solution of FS-FEM using a very fine mesh including 17,988 degrees of freedom and 30,168 elements is used as reference solution. The results again verify that the FS-FEM model is softer and gives more accurate results than the FEM model using tetrahedral elements.

4.4. A 3D Cook's membrane: visco-elastoplasticity with linear kinematic hardening

Fig. 25 show a 3D Cook's membrane on  $yOz$  plane, and a discretization of the domain using 2317 nodes and 9583 tetrahedral elements. At the high end of the membrane, there is a time dependent shear force  $g = 90te_z$  and the other end is fixed. Assuming that the material is visco-elastoplasticity with linear kinematic hardening with Young's modulus  $E = 70,000$ , Poisson's ratio  $\nu = 0.3$ , yield stress  $\sigma_Y = 400$ , hardening parameter  $k_1 = 2$ , and the initial data for the displacement  $u_0$ , the stress tensor  $\sigma_0$  and the hardening parameter  $\alpha_0^k$  are set zero.

The solution is calculated in the time interval from  $t = 0$  to  $t = 1.0$  in 10 uniform steps  $\Delta t = 0.1$ . Using the mesh as shown in Fig. 25, the material remains elastic in five first steps, between  $t = 0$  and  $t = 0.5$  for both the FS-FEM and FEM as shown in Table 5. Table 5 also shows that the number of iterations in Newton's method of both the FS-FEM and FEM are almost the same, but the estimated errors  $\eta^h$  in Eq. (56) of FS-FEM are about 30% less than those of FEM. In addition, Fig. 26 compares the computational cost and efficiency between the FEM and FS-FEM for a range of meshes at  $t = 1$ . It is seen that with the same mesh, the computational cost of FS-FEM is larger than that of FEM as shown in Fig. 26a. However, when the efficiency of computation (computation time for the same accuracy) in terms of the error estimator versus computational cost for a range of meshes is considered, the FS-FEM is more efficient than the FEM as shown in Fig. 26b.

Fig. 27 shows the elastic shear energy density  $\|\text{dev}(\mathbf{R}\sigma^h)\|^2/(4\mu)$  at  $t = 1.0$  which is almost the same for the FEM and FS-FEM. The evolution of the elastic shear energy density  $\|\text{dev}(\mathbf{R}\sigma^h)\|^2/(4\mu)$  is demonstrated using the FS-FEM at four different time instances as shown in Fig. 28 in which the plastic domain first appears at the fixed upper corner and then at the middle part of the lower boundary face.

Fig. 29 shows the convergence of the elastic strain energy  $E = \int_{\Omega} \sigma_{ij} : \epsilon_{ij} d\Omega$  versus the number of degrees of freedom using the FEM and FS-FEM at  $t = 1.0$ . The solution of FS-FEM using a very fine mesh including 17,307 degrees of freedom and 26,084 elements is used as reference solution. The results again verify that the FS-FEM model is softer and gives more accurate results than the FEM model using tetrahedral elements.

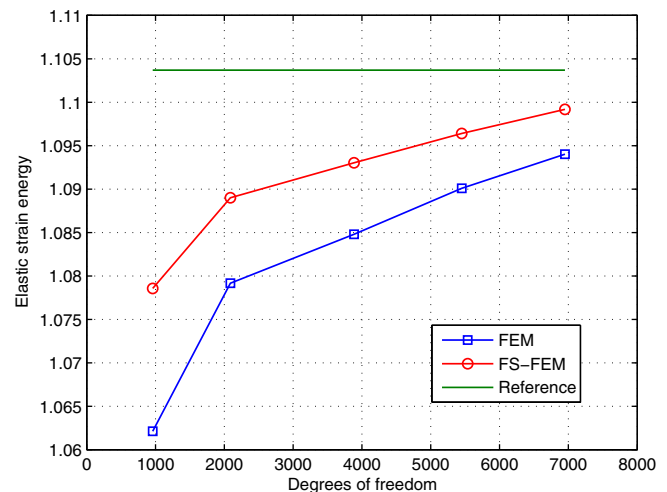


Fig. 29. Convergence of the elastic strain energy  $E = \int_{\Omega} \sigma_{ij} : \epsilon_{ij} d\Omega$  versus the number of degrees of freedom at  $t = 1$  of the 3D Cook's membrane problem.

## 5. Conclusion

In this paper, the FS-FEM is extended to more complicated visco-elastoplastic analyses in 3D solids. We combine the FS-FEM using tetrahedral elements with the work of Carstensen and Klose [50] in the setting of von-Mises conditions and the Prandtl–Reuss flow rule, and the material behavior includes perfect visco-elastoplasticity, and visco-elastoplasticity with isotropic hardening and linear kinematic hardening in a dual model, with displacements and the stresses as the main variables. The numerical procedure, however, eliminates the stress variables and the problem becomes only displacement-dependent and is easier to deal with. The numerical results of FS-FEM using tetrahedral elements show that

- The bandwidth of stiffness matrix of FS-FEM is larger than that of FEM, and hence the computational cost of FS-FEM is larger than that of FEM. However, when the efficiency of computation (computation time for the same accuracy) in terms of a posteriori error estimation is considered, the FS-FEM is more efficient than FEM.
- The displacement results of FS-FEM are larger than those of FEM. The elastic strain energy of FS-FEM is more accurate than that of FEM. These results show clearly that the FS-FEM model can reduce the over-stiffness of the standard FEM model using tetrahedral elements and gives more accurate results than those of FEM.
- For the axis-symmetric problems, the results of FS-FEM are more symmetric than those of FEM.

## Acknowledgements

This work is partially supported by a \*Star, Singapore. It is also partially supported by the Open Research Fund Program of the State Key Laboratory of Advanced Technology of Design and Manufacturing for Vehicle Body, Hunan University, P.R.China under the grant number 40915001.

## References

- [1] G.R. Liu, *Meshfree Methods: Moving Beyond the Finite Element Method*, second ed., Taylor & Francis/CRC Press, Boca Raton, USA, 2009.
- [2] G.R. Liu, A G space theory and weakened weak (W2) form for a unified formulation of compatible and incompatible methods: part I theory, part II application to solid mechanics problems, *Int. J. Numer. Methods Engrg.*, in press.
- [3] J.S. Chen, C.T. Wu, S. Yoon, Y. You, A stabilized conforming nodal integration for Galerkin meshfree method, *Int. J. Numer. Methods Engrg.* 50 (2001) 435–466.
- [4] J.W. Yoo, B. Moran, J.S. Chen, Stabilized conforming nodal integration in the natural-element method, *Int. J. Numer. Methods Engrg.* 60 (2004) 861–890.
- [5] G.R. Liu, A generalized gradient smoothing technique and the smoothed bilinear form for Galerkin formulation of a wide class of computational methods, *Int. J. Comput. Methods* 5 (2) (2008) 199–236.
- [6] T.P. Fries, H.G. Matthies, *Classification and Overview of Meshfree Methods*, Institute of Scientific Computing, Technical University Braunschweig, Germany, Informatikbericht.
- [7] V.P. Nguyen, T. Rabczuk, B. Bordas, M. Duflot, Meshless methods: review and key computer implementation aspects, *Math. Comput. Simul.* 79 (2008) 763–813.
- [8] S. Bordas, T. Rabczuk, G. Zi, Three-dimensional crack initiation, propagation, branching and junction in non-linear materials by an extended meshfree method without asymptotic enrichment, *Eng. Fract. Mech.* 75 (5) (2008) 943–960.
- [9] T. Rabczuk, T. Belytschko, Cracking particles: a simplified meshfree method for arbitrary evolving cracks, *Int. J. Numer. Methods Engrg.* 61 (13) (2004) 2316–2343.
- [10] T. Rabczuk, T. Belytschko, S.P. Xiao, Stable particle methods based on Lagrangian kernels, *Comput. Methods Appl. Mech. Engrg.* 193 (2004) 1035–1063.
- [11] T. Rabczuk, S. Bordas, G. Zi, A three-dimensional meshfree method for continuous multiple-crack initiation, propagation and junction in statics and dynamics, *Comput. Mech.* 40 (3) (2007) 473–495.
- [12] T. Rabczuk, T. Belytschko, A three-dimensional large deformation meshfree method for arbitrary evolving cracks, *Comput. Methods Appl. Mech. Engrg.* 196 (2007) 2777–2799.
- [13] T. Rabczuk, G. Zi, S. Bordas, H. Nguyen-Xuan, A geometrically non-linear three-dimensional cohesive crack method for reinforced concrete structures, *Eng. Fract. Mech.* 75 (16) (2008) 4740–4758.
- [14] G.R. Liu, G.Y. Zhang, K.Y. Dai, Y.Y. Wang, Z.H. Zhong, G.Y. Li, X. Han, A linearly conforming point interpolation method (LC-PIM) for 2D solid mechanics problems, *Int. J. Comput. Methods* 2 (4) (2005) 645–665.
- [15] G.R. Liu, G.Y. Zhang, Y.Y. Wang, H.T. Huang, Z.H. Zhong, G.Y. Li, X. Han, A linearly conforming point interpolation method (LC-PIM) for three-dimensional elasticity problems, *Int. J. Numer. Methods Engrg.* 72 (2007) 1524–1543.
- [16] G.R. Liu, Y. Li, K.Y. Dai, M.T. Luan, W. Xue, A linearly conforming radial point interpolation method for solid mechanics problems, *Int. J. Comput. Methods* 3 (4) (2006) 401–428.
- [17] G.R. Liu, K.Y. Dai, T. Nguyen-Thoi, A smoothed finite element method for mechanics problems, *Comput. Mech.* 39 (2007) 859–877.
- [18] G.R. Liu, T. Nguyen-Thoi, K.Y. Dai, K.Y. Lam, Theoretical aspects of the smoothed finite element method (SFEM), *Int. J. Numer. Methods Engrg.* 71 (2007) 902–930.
- [19] Hung Nguyen-Xuan, Stéphane Bordas, Hung Nguyen-Dang, Smooth finite element methods: convergence, accuracy and properties, *Int. J. Numer. Methods Engrg.* 74 (2008) 75–208.
- [20] G.R. Liu, T. Nguyen-Thoi, H. Nguyen-Xuan, K.Y. Dai, K.Y. Lam, On the essence and the evaluation of the shape functions for the smoothed finite element method (SFEM) (letter to editor), *Int. J. Numer. Methods Engrg.* 77 (2009) 1863–1869.
- [21] G.R. Liu, T. Nguyen-Thoi, H. Nguyen-Xuan, K.Y. Lam, A node-based smoothed finite element method for upper bound solution to solid problems (NS-FEM), *Comput. Struct.* 87 (2009) 14–26.
- [22] G.R. Liu, T. Nguyen-Thoi, K.Y. Lam, An edge-based smoothed finite element method (ES-FEM) for static, free and forced vibration analyses of solids, *J. Sound Vib.* 320 (2009) 1100–1130.
- [23] H. Nguyen-Xuan, G.R. Liu, T. Nguyen-Thoi, C. Nguyen-Tran, An edge-based smoothed finite element method (ES-FEM) for analysis of two-dimensional piezoelectric structures, *Smart Mater. Struct.* 18 (2009) 065015. 12p.
- [24] T. Nguyen-Thoi, G.R. Liu, H.C. Vu-Do, H. Nguyen-Xuan, An edge-based smoothed finite element method (ES-FEM) for visco-elastoplastic analyses in 2D solids mechanics using triangular mesh, *Comput. Mech.*, 2009, in press.
- [25] H. Nguyen-Xuan, G.R. Liu, C. Thai-Hoang, T. Nguyen-Thoi, An edge-based smoothed finite element method with stabilized discrete shear gap technique for analysis of Reissner–Mindlin plates, *Comput. Methods Appl. Mech. Engrg.*, 2009, submitted for publication.
- [26] Thanh Ngoc Tran, G.R. Liu, H. Nguyen-Xuan, T. Nguyen-Thoi, An edge-based smoothed finite element method for primal-dual shakedown analysis of structures, *Int. J. Numer. Methods Engrg.*, 2009 (Revised).
- [27] S.P. A. Bordas, T. Rabczuk, N.X. Hung, V.P. Nguyen, S. Natarajan, T. Bog, D.M. Quan, N.V. Hiep, Strain smoothing in FEM and XFEM, *Comput. Struct.* (2009), doi:10.1016/j.compstruc.2008.07.006.
- [28] K.Y. Dai, G.R. Liu, T. Nguyen-Thoi, An n-sided polygonal smoothed finite element method (nSFEM) for solid mechanics, *Finite Elements Anal. Des.* 43 (2007) 847–860.
- [29] K.Y. Dai, G.R. Liu, Free and forced analysis using the smoothed finite element method (SFEM), *J. Sound Vib.* 301 (2007) 803–820.
- [30] T. Nguyen-Thoi, G.R. Liu, K.Y. Dai, K.Y. Lam, Selective smoothed finite element method, *Tsinghua Sci. Technol.* 12 (5) (2007) 497–508.
- [31] H. Nguyen-Xuan, S. Bordas, H. Nguyen-Dang, Addressing volumetric locking and instabilities by selective integration in smoothed finite elements, *Commun. Numer. Methods Engrg.* 25 (2008) 19–34.
- [32] H. Nguyen-Xuan, T. Nguyen-Thoi, A stabilized smoothed finite element method for free vibration analysis of Mindlin–Reissner plates, *Commun. Numer. Methods Engrg.* 25 (2009) 882–906.
- [33] X.Y. Cui, G.R. Liu, G.Y. Li, X. Zhao, T. Nguyen-Thoi, G.Y. Sun, A smoothed finite element method (SFEM) for linear and geometrically nonlinear analysis of plates and shells, *CMES – Comput. Model. Engrg. Sci.* 28 (2) (2008) 109–125.
- [34] N. Nguyen-Thanh, T. Rabczuk, H. Nguyen-Xuan, S. Bordas, A smoothed finite element method for shell analysis, *Comput. Methods Appl. Mech. Engrg.* 198 (2008) 165–177.
- [35] H. Nguyen-Van, N. Mai-Duy, T. Tran-Cong, A smoothed four-node piezoelectric element for analysis of two-dimensional smart structures, *CMES – Comput. Model. Engrg. Sci.* 23 (3) (2008) 209–222.
- [36] H. Nguyen-Xuan, T. Rabczuk, S. Bordas, J.F. Debonnie, A smoothed finite element method for plate analysis, *Comput. Methods Appl. Mech. Engrg.* 197 (2008) 1184–1203.
- [37] S. Bordas, T. Rabczuk, H. Nguyen-Xuan, P. Nguyen Vinh, S. Natarajan, T. Bog, Q. Do Minh, H. Nguyen Vinh, Strain smoothing in FEM and XFEM, *Comput. Struct.* (2009), doi:10.1016/j.compstruc.2008.07.006.
- [38] N. Sukumar, E.A. Malsch, Recent advances in the construction of polygonal finite element interpolants, *Arch. Comput. Methods Engrg.* 13 (1) (2006) 129–163.
- [39] N. Sukumar, A. Tabarraei, Conforming polygonal finite elements, *Int. J. Numer. Methods Engrg.* 61 (2004) 2045–2066.
- [40] N. Sukumar, Construction of polygonal interpolants: a maximum entropy approach, *Int. J. Numer. Methods Engrg.* 61 (2004) 2159–2181.

- [41] S. Natarajan, S. Bordas, D.R. Mahapatra, Numerical integration over arbitrary polygonal domains based on Schwarz–Christoffel conformal mapping, *Int. J. Numer. Methods Eng.* (2009), doi:10.1002/nme.
- [42] C.R. Dohrmann, M.W. Heinstein, J. Jung, S.W. Key, W.R. Witkowski, Node-based uniform strain elements for three-node triangular and four-node tetrahedral meshes, *Int. J. Numer. Methods Engrg.* 47 (2000) 1549–1568.
- [43] G.R. Liu, G.Y. Zhang, Upper bound solution to elasticity problems: a unique property of the linearly conforming point interpolation method (LC-PIM), *Int. J. Numer. Methods Engrg.* 74 (2008) 1128–1161.
- [44] G.R. Liu, T. Nguyen-Thoi, K.Y. Lam, A novel alpha finite element method ( $\alpha$ FEM) for exact solution to mechanics problems using triangular and tetrahedral elements, *Comput. Methods Appl. Mech. Engrg.* 197 (2008) 3883–3897.
- [45] A.J. Aref, Z. Guo, Framework for finite-element-based large increment method for nonlinear structural problems, *J. Engrg. Mech.* 127 (2001) 739–746.
- [46] S.N. Patnak, The integrated force method versus the standard force method, *Comput. Struct.* 22 (1986) 151–163.
- [47] B.F. Veubeke, Displacement and equilibrium models in the finite element method, in: O.C. Zienkiewicz, G.S. Holister (Eds.), *Stress Analysis*, Wiley, London, 1965.
- [48] T. Nguyen-Thoi, G.R. Liu, H. Nguyen-Xuan, C. Nguyen-Tran, Adaptive analysis using the node-based smoothed finite element method (NS-FEM), *Commun. Numer. Methods Engrg.* (2009), doi:10.1002/cnm.1291.
- [49] T. Nguyen-Thoi, G.R. Liu, K.Y. Lam, G.Y. Zhang, A face-based smoothed finite element method (FS-FEM) for 3D linear and nonlinear solid mechanics problems using 4-node tetrahedral elements, *Int. J. Numer. Methods Engrg.* 78 (2009) 324–353.
- [50] C. Carstensen, R. Klose, Elastoviscoplastic finite element analysis in 100 lines of matlab, *J. Numer. Math.* 10 (2002) 157–192.
- [51] C. Carstensen, S.A. Funken, Averaging technique for FE-a posteriori error control in elasticity. Part 1: conforming FEM, *Comput. Methods Appl. Mech. Engrg.* 190 (2001) 2483–2498.
- [52] M. Duflot, S. Bordas, A posteriori error estimation for extended finite elements by an extended global recovery, *Int. J. Numer. Methods Engrg.* 76 (2008) 1123–1138.
- [53] S. Bordas, M. Duflot, Derivative recovery and a posteriori error estimate for extended finite elements, *Comput. Methods Appl. Mech. Engrg.* 196 (2007) 3381–3399.
- [54] S. Bordas, M. Duflot, P. Le, A simple error estimator for extended finite elements, *Commun. Numer. Methods Engrg.* 24 (2008) 961–971.
- [55] J.J. Rodenas, O.A. Gonzalez-Estrada, J.E. Tarancon, F.J. Fuenmayor, A recovery-type error estimator for the extended finite element method based on singular + smooth stress field splitting, *Int. J. Numer. Methods Engrg.* 76 (2008) 545–571.
- [56] T. Rabczuk, T. Belytschko, Adaptivity for structured meshfree particle methods in 2D and 3D, *Int. J. Numer. Methods Engrg.* 63 (2005) 1559–1582.
- [57] T. Pannachet, L.J. Sluys, H. Askes, Error estimation and adaptivity for discontinuous failure, *Int. J. Numer. Methods Engrg.* 78 (2008) 528–563.